A Fourier-spectral element algorithm for thermal convection in rotating axisymmetric containers

Alexandre Fournier [a,*], Hans-Peter Bunge [a,1], Rainer Hollerbach [b],
Jean-Pierre Vilotte [c]

[a] *Department of Geosciences, Guyot Hall, Princeton University, Princeton, NJ 08544, USA*
[b] *Department of Mathematics, University of Glasgow, Glasgow G12 8QW, UK*
[c] *Département de Modélisation Physique et Numérique, Institut de Physique du Globe de Paris, 4 Place Jussieu,
75252 Paris Cedex 05, France*

Abstract

We present a Fourier-spectral element approach for modeling thermal convection in a rotating axisymmetric container. Following the theory detailed in Bernardi et al. [C. Bernardi, M. Dauge, Y. Maday, Spectral Methods for Axisymmetric Domains, Gauthier-Villars, Paris, 1999], a Fourier expansion of the field variables is performed in the periodic direction, and the resulting collection of meridional problems is discretized by means of a parallel spectral element method. A Gauss–Lobatto–Jacobi (0,1) quadrature, which incorporates the cylindrical radius in its weight, is introduced to avoid a potential degeneracy of the discrete set of equations, due to those nodes located on the axis of symmetry. A second-order timestepping scheme is presented, which treats the Coriolis and viscous forces implicitly. Numerical comparisons with analytical and published numerical solutions in spherical and cylindrical geometries are presented which highlight the accuracy of the model and demonstrate its spectral convergence properties.
© 2004 Elsevier Inc. All rights reserved.

Keywords: Rotating fluids; Boussinesq equations; Fourier-spectral element method; Cylindrical coordinates; Pole conditions

---

[*] Corresponding author. Present address: Geodynamo Team, Internal Geophysics and Tectonophysics Laboratory (LGIT), BP 53, 38000 Grenoble, France. Tel.: +33 4 76 82 80 27.
E-mail address: Alexandre.Fournier@ujf-grenoble.fr (A. Fournier).
[1] Present address: Department of Earth and Environmental Sciences, Geophysics Section, Ludwig-Maximilians-Universität München, Theresienstraße 41, 80333 München, Germany.

1. Introduction

Large-scale planetary fluid flows are strongly influenced by the background rotation of planetary bodies. On Earth, the effects of the Coriolis force in the atmosphere and in the oceans are observed (and monitored) on an hourly basis. At the same time, geological records of the magnetic field of the Earth (generated inside its liquid iron outer core through dynamo action) indicate that the geomagnetic field is on average parallel (or anti-parallel) to the North–South axis [1]. Each terrestrial fluid layer is therefore very sensitive on its own timescales to the Earth's rotation ω. This reflects the importance of the so-called geostrophic equilibrium, in which the Coriolis force $2\rho\omega \times \mathbf{u}$ (where ρ and $\mathbf{u}$ are the fluid density and velocity, respectively) is balanced by the pressure gradient ∇p:

$$2\rho\omega \times \mathbf{u} = -\nabla p. \tag{1}$$

Taking the curl of this balance leads to

$$2\omega(\hat{\mathbf{z}}\nabla \cdot \mathbf{u} - \partial_z\mathbf{u}) = \frac{1}{\rho}\nabla\rho \times \nabla p, \tag{2}$$

where $\hat{\mathbf{z}}$ is the unit vector in the direction of rotation ($\omega = \omega\hat{\mathbf{z}}$). Throughout this paper, (x,y,z), (s,ϕ,z), and (r,θ,ϕ) will denote Cartesian, cylindrical, and spherical coordinates, respectively.

If we further assume that the fluid has a constant density $\rho = \rho_0$, we obtain the so-called Taylor–Proudman theorem

$$\partial_z\mathbf{u} = \mathbf{0}. \tag{3}$$

This theorem implies that a fast rotation introduces a substantial amount of anisotropy in the flow, which tends to be invariant along the direction of rotation; the flow is organized in a columnar fashion, the columns being parallel to the z-axis.

Deviations from a geostrophic state arise from the (re)introduction of other dynamical ingredients in the momentum equation. Viscous forces are for instance required if no-slip boundary conditions are to be applied. They are responsible for the generation of sharp Edmon boundary layers, in which there is a local equilibrium between the Coriolis force, the pressure gradient and the viscous force. Moreover, inertia induces the existence of a class of fast oscillations called inertial waves, the frequency of which is smaller than 2ω [2]. A departure from a geostrophic equilibrium can also occur when a large enough body force is applied to the fluid. For instance, thermal heterogeneities in a viscous fluid can drive non-geostrophic motion. In a classical paper, Busse [3] showed that thermal instabilities in a sphere took the form of a drifting sequence of narrow columns parallel to the axis of rotation. In particular, he demonstrated that the critical longitudinal wave number k_c characterizing this "banana belt" instability varies in the rapidly rotating limit as $\omega^{1/3}$: the larger the rotation rate, the smaller the equatorial extent of the so-called Busse columns. On a similar note, in the case of metallic planetary cores, this body force can be the Lorentz force, the feedback from the magnetic field on the fluid flow. The balance between Coriolis force, pressure force, and the Lorentz force is called the magnetostrophic balance [4].

Having in mind on the long run to design a model able to simulate flows in planetary cores, our objective in this paper is to present a numerical formulation to solve thermal convection for a non-magnetic viscous fluid, in the framework of the Boussinesq approximation and in the rapidly rotating limit. We present for the time the application of a Fourier-spectral element approximation of the relevant equations, in conjunction with a timemarching scheme that treats the effects of rotation implicitly. This work represents the first implementation of the theoretical foundations laid by Bernardi et al. [5] to nonlinear problems relevant for such geophysical flows.

Because of its relevance for planetary and stellar studies, this problem has received considerable attention from modelers over the past thirty years. The most successful attempts for numerical simulations of

geophysical flows in rotating spherical shells to date are based upon spectral transform methods (STM) which expand the variables of interest on the two-sphere upon the global basis of spherical harmonics, while Chebyshev collocation or finite-differences are generally used in radius [6–10]. Time integration is performed in spectral space using a Courant limited numerical time step, and nonlinear terms are computed at each time step by transforming functions back into grid space (typically a latitude–longitude structured grid), in which nonlinear products are computed. A large body of work has grown, addressing the problem of efficient and stable computation of scalar spherical harmonic transforms [11–13], as well as of harmonic transforms for vector and tensor fields on the two-sphere [14,15]. However, STM still suffer from some drawbacks. In particular, they are restricted to spherical geometry. Aspherical geometrical features can be introduced only through a perturbative approach (assuming therefore a small deviation from sphericity) or an involved coordinate transform – to model for instance flows in spheroidal shells [16]. Moreover, in the rapidly rotating limit, the implicit treatment of the Coriolis force, which allows to control inertial waves, couples spherical harmonics coefficients and has a severe impact on memory requirements [9]. Finally, in order to reach high resolution, parallel processing is necessary, the efficiency of which is penalized by communication overheads.

This last issue arises from the fact that spherical harmonics are tensor products of combinations of Fourier series in longitude with associated Legendre functions in latitude. Despite recent improvements, no fast discrete spherical transform exists and the transform requires $\mathcal{O}(L^3)$ operations [17], if L denotes the largest spherical harmonic degree. This corresponds to a computational effort of $\mathcal{O}(L^4)$ in three dimensions, assuming that roughly the same resolution is adopted in the vertical direction as on the two-sphere. At high resolution, the transforms become the main part of the computations – more than 80% of the total CPU in Kuang and Bloxham's three-dimensional (3D) dynamo model [7]. On distributed memory architectures, the global nature of the STM imposes overhead in the communications between processors that becomes critical as L increases. We should mention, however, a recent and successful effort by Clune et al. [18] who developed a highly efficient parallel implementation on the CRAY T3E of a STM code originally written by Glatzmaier [6].

Aside from STM approaches, a growing number of studies have been conducted toward grid-based numerical methods in spherical geometries. Most of them are based upon finite differences (FD) [19,20] or pseudo-spectral [21] methods formulated in cylindrical or spherical coordinates. FD methods are penalized by grid dispersion near strong gradients and require a large number of grid points to achieve the expected accuracy. Higher-order methods, like pseudo-spectral methods, are able to reach the expected accuracy using fewer grid points [22]. The major problem of these methods is that they fail to provide a uniform representation of scalar functions on the two-sphere. Latitude–longitude grids are indeed highly non-isotropic with a clustering of points near the poles that leads to severe timestep restrictions [23, Section 18.10]. These methods have nevertheless some advantages, not only in terms of storage and periodicity, but also in terms of efficient calculation of spatial derivatives on the two-sphere that take advantage of the structure of a latitude–longitude grid. One such approach, previously proposed by Merilees [24], which uses fast Fourier transforms (FFT) on circles on the sphere, has been recently revisited [21,25] and shown to be quite accurate when used in conjunction with suitable spectral filters [26,27]. It has been applied to the shallow water equations, and remains to be explored in the context of planetary cores dynamics, for which the thin shell approximation is no longer valid.

Other promising grid-based methods stem from the variational formulation of the momentum and energy equations and include the finite element method (FEM) and the spectral element method (SEM), using spherical geodesic grids generated either from the tiling of an icosahedron [28–31] or a gnomic projection – the so-called "cubed sphere" [32–35]. The 3D mesh of a spherical shell is obtained by radially connecting the quadrangles between two concentric cubed spheres. The discretization of a whole sphere can then be completed if needed by inscribing a cube at the center with a smooth transition [36]. Such a discretization provides a uniform tilling of the two-sphere avoiding classical pole problems of spherical and cylindrical coordinates and the singularity at the center of the sphere is naturally removed.

The SEM is specifically quite appealing: it has now become customary to highlight that it combines the geometrical flexibility of conventional finite element methods with the exponential convergence rate associated with spectral techniques [37]. Efficient parallelization can be achieved on distributed memory architecture and excellent scalings have been measured as far as explicit time schemes are involved [38]. The SEM yields a $\mathcal{O}(n_e N^{d+1})$ complexity, where n_e is the number of elements, N refers here to the polynomial degree used in each direction inside each element, and d is the number of spatial dimensions. Since the ratio of the number of elements n_e to N can be controlled, N is generally much smaller than the maximum degree L of spherical harmonics in STM models and the cost of the transforms is kept in line with the rest of the model. The SEM has the disadvantage, though, that it gives rise to linear operators which are difficult to invert if one uses semi-implicit or fully implicit schemes (essential in the rapidly rotating limit). This statement is particularly relevant for the elliptic operator that must be inverted to compute the pressure increment in pressure correction schemes. Iterative methods with efficient preconditioners are required that permit an efficient parallel implementation. This is not a trivial task, especially in three dimensions [39].

The purpose of this paper is to introduce and validate an efficient and accurate implicit spectral element-based method to simulate convection in rotating spherical or ellipsoidal geometries. In order to keep the numerical complexity of the problem as low as possible, we set the problem in cylindrical coordinates (the set of coordinates naturally associated with the Taylor–Proudman theorem) and make use of the 2π natural periodicity in longitude for spherical and ellipsoidal geometries, by expanding the physical variables in Fourier series in ϕ. This leads to $K + 1$ coupled two-dimensional problems written in the meridional plane, where K is the highest Fourier angular mode retained in the expansion. These problems are coupled only through the nonlinear terms, while no extra coupling arises from the linear rotation (Coriolis) term, since the axis of rotation does coincide with the z-axis of the cylindrical coordinates set. This method, hereafter referred to as the Fourier-spectral element method (FSEM), provides substantial simplifications in terms of implementation and mesh design, thanks to the dimension reduction and the elimination of the angular curvature. Let us stress here that the methodology presented in this paper is valid for any kind of 3D domain with axial symmetry.

A brief description of the governing equations in the 3D domain is provided in Section 2. In Section 3, we reformulate the problem in cylindrical coordinates and reduce its dimension by performing a Fourier expansion in longitude, which gives rise to a collection of problems to solve in the meridional plane. In Section 4, the variational formulation of each problem is given and the requirements that fields have to meet on the axis of symmetry are reviewed. In Section 5, we describe the extensions required for the standard SEM to handle both the Fourier discretization with respect to the angular variable (longitude) and the weighted measure due to the cylindrical coordinates system; we resort to a Gauss–Lobatto–Jacobi (0,1) quadrature in the direction orthogonal to the axis of symmetry for elements that touch this axis. Furthermore, velocity and pressure are approximated by means of a $P_N - P_{N-2}$ approach. Section 6 describes in detail the time discretization and the fractional step method used to advance the model in time. In particular, as advocated by Perot [40], the splitting is done at the algebraic level, and, thanks to the $P_N - P_{N-2}$ approach, any reference to boundary conditions for pressure is bypassed, thereby avoiding the possible generation of divergence boundary layers. Finally, in Section 7, we present two sets of numerical comparisons with analytical and/or numerical solutions in spherical or cylindrical geometries, which highlight the accuracy and the spectral convergence properties of the FSEM. We end the paper with some concluding remarks and perspectives, and provide in the appendix details on the removal of the apparent axial singularities.

2. Governing equations

Consider a homogeneous Newtonian convecting fluid of density ρ, kinematic viscosity v and thermal diffusivity κ, embedded in an axially symmetric container $\breve{\Omega}$ which can be rotating about its axis of symmetry

at constant angular velocity ω (see Fig. 1). Let $\hat{\mathbf{z}}$ denote the unit vector in the direction of rotation. We assume that motion is driven by thermal anomalies only and choose the following length and time scales:

$$[L] \sim a, \quad [t] \sim a^2/v, \tag{4}$$

in which a is a typical dimension of the container. Accordingly, v/a and $\rho v^2/a^2$ are the velocity and pressure scales.

In the framework of the Boussinesq approximation [41], the nondimensional conservations of mass, momentum and energy write respectively

$$\nabla \cdot \mathbf{u} = 0, \tag{5a}$$

$$\partial_t \mathbf{u} + \mathbf{u} \cdot \nabla \mathbf{u} + 2C\hat{\mathbf{z}} \times \mathbf{u} + \nabla P = \nabla^2 \mathbf{u} + \mathbf{f}(T), \tag{5b}$$

$$\partial_t T + \mathbf{u} \cdot \nabla T = \frac{1}{Pr}\nabla^2 T - \mathbf{u} \cdot \nabla T_s, \tag{5c}$$

where $\mathbf{u}$ is the fluid velocity, P is the pressure perturbation, T is the temperature anomaly, and T_s is the static (conductive) temperature distribution. We assume that this set of equations is supplemented by suitable initial conditions and by homogeneous Dirichlet boundary conditions for velocity and temperature anomaly on the boundary of the container $\partial\breve{\Omega}$. These correspond physically to no-slip conditions for fluid flow and an imposed temperature on $\partial\breve{\Omega}$. Note that the implementation of stress-free and thermally insulating boundary conditions require only slight modifications of the implementation described in what follows.

The Coriolis number

$$C = \frac{a^2\omega}{v} \tag{6}$$

expresses the relative importance of rotational versus viscous effects. It is the inverse of the Ekman number

$$Ek = \frac{v}{a^2\omega}, \tag{7}$$

the use of which is more frequent in geophysical fluid dynamics [2]. The rapidly rotating limit corresponds to $C \gg 1$, or equivalently, $Ek \ll 1$.

The explicit expression of $\mathbf{f}$ in Eq. (5b) depends on the problem of interest. It is typically of the form
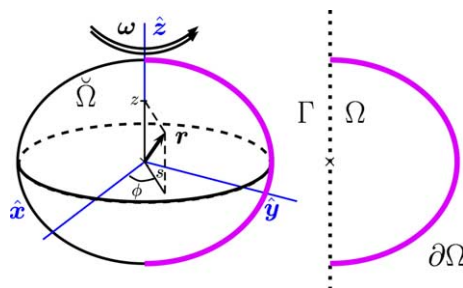
$$\mathbf{f}(T) = -RT\hat{\mathbf{g}}, \tag{8}$$

Fig. 1. The three-dimensional domain $\breve{\Omega}$ (in this example an oblate spheroid) is axially symmetric about the axis Γ and can rotate about this axis at a rate ω. We denote the meridional section of $\breve{\Omega}$ with Ω, and its meridional boundary with $\partial\Omega$. Cylindrical coordinates are denoted with (s,ϕ,z), with the z-axis aligned with the axis of symmetry.

in which $\hat{\mathbf{g}}$ is the unit vector parallel to the gravity field and R is the (nondimensional) Rayleigh number. The Rayleigh number is a measure of the vigor of convection and its expression depends on the physical properties of the fluid of interest (thermal diffusivity, coefficient of thermal expansion, kinematic viscosity), on the strength of gravity, and on the thermal scale chosen. This thermal scale is related to the basic (conductive) thermal state T_s which depends in turn on the thermal boundary conditions, and on the presence of internal heat sources h_s. For the sake of clarity, we will ignore these subtleties throughout the discussion of the numerical method. We shall, however, provide an explicit expression for $\mathbf{f}(T)$ and R when dealing with the rotating convection example of Section 7.

Finally, Pr in Eq. (5c) is the Prandtl number

$$Pr = \frac{v}{\kappa}, \tag{9}$$

the ratio of viscous diffusivity to thermal diffusivity.

3. Strong cylindrical form – problem reduction by a Fourier expansion in longitude

The axisymmetry of $\breve{\Omega}$, as well as the Proudman–Taylor theorem (3) in the rapidly rotating situation, favors the use of a (s,ϕ,z) system of cylindrical coordinates (see Fig. 1). The dependence in ϕ can then be accounted for through a Fourier expansion, which breaks the original three-dimensional problem in a collection of two-dimensional ones.

If (u_s,u_ϕ,u_z) denote the three cylindrical components of velocity, then set (5a) can be written as

$$\partial_s u_s + \frac{1}{s}u_s + \frac{1}{s}\partial_\phi u_\phi + \partial_z u_z = 0, \tag{10a}$$

$$\partial_t u_s - 2Cu_\phi + \partial_s P = \nabla^2 u_s - \frac{u_s}{s^2} - \frac{2}{s^2}\partial_\phi u_\phi + b_s, \tag{10b}$$

$$\partial_t u_\phi + 2Cu_s + \frac{\partial_\phi P}{s} = \nabla^2 u_\phi - \frac{u_\phi}{s^2} + \frac{2}{s^2}\partial_\phi u_s + b_\phi, \tag{10c}$$

$$\partial_t u_z + \partial_z P = \nabla^2 u_z + b_z, \tag{10d}$$

$$\partial_t T = \frac{1}{Pr}\nabla^2 T + b_T, \tag{10e}$$

in which

$$b_s = f_s - \left(u_s\partial_s u_s + \frac{u_\phi}{s}\partial_\phi u_s + u_z\partial_z u_s - \frac{u_\phi^2}{s}\right), \tag{11}$$

$$b_\phi = f_\phi - \left(u_s\partial_s u_\phi + \frac{u_\phi}{s}\partial_\phi u_\phi + u_z\partial_z u_\phi + \frac{u_s u_\phi}{s}\right), \tag{12}$$

$$b_z = f_z - \left(u_s\partial_s u_z + \frac{u_\phi}{s}\partial_\phi u_z + u_z\partial_z u_z\right), \tag{13}$$

$$b_T = -\left(u_s\partial_s + \frac{u_\phi}{s}\partial_\phi + u_z\partial_z\right)(T + T_s). \tag{14}$$

The expression of the scalar Laplacian operator ∇^2 in cylindrical coordinates is

$$\nabla^2 = \partial_s^2 + \frac{1}{s}\partial_s + \frac{1}{s^2}\partial_\phi^2 + \partial_z^2. \tag{15}$$

We now perform a Fourier expansion of the field variables in the longitudinal direction

$$\{\mathbf{u}, P, T, b_T, \mathbf{b}\} = \sum_{k=-\infty}^{k=+\infty} \left\{ \tilde{\mathbf{u}}^k, \tilde{P}^k, \tilde{T}^k, \tilde{b}_T^k, \tilde{\mathbf{b}}^k \right\} e^{ik\phi}. \tag{16}$$

This expansion, when inserted in problem (10), leads to a series of meridional problems $\mathscr{P}^k$ to solve in Ω for each Fourier mode k

$$\partial_s \tilde{u}_s^k + \frac{1}{s}\tilde{u}_s^k + \frac{ik}{s}\tilde{u}_\phi^k + \partial_z \tilde{u}_z^k = 0, \tag{17a}$$

$$\partial_t \tilde{u}_s^k - 2C\tilde{u}_\phi^k + \partial_s \tilde{P}^k = \nabla_k^2 \tilde{u}_s^k - \frac{1}{s^2}\tilde{u}_s^k - \frac{2ik}{s^2}\tilde{u}_\phi^k + \tilde{b}_s^k, \tag{17b}$$

$$\partial_t \tilde{u}_\phi^k + 2C\tilde{u}_s^k + \frac{ik}{s}\tilde{P}^k = \nabla_k^2 \tilde{u}_\phi^k - \frac{1}{s^2}\tilde{u}_\phi^k + \frac{2ik}{s^2}\tilde{u}_s^k + \tilde{b}_\phi^k, \tag{17c}$$

$$\partial_t \tilde{u}_z^k + \partial_z \tilde{P}^k = \nabla_k^2 \tilde{u}_z^k + \tilde{b}_z^k, \tag{17d}$$

$$\partial_t \tilde{T}^k = \frac{1}{Pr}\nabla_k^2 \tilde{T}^k + \tilde{b}_T^k. \tag{17e}$$

The scalar Laplacian ∇_k^2 is a function of k:

$$\nabla_k^2 = \partial_s^2 + \frac{1}{s}\partial_s - \frac{k^2}{s^2} + \partial_z^2. \tag{18}$$

Introducing

$$\nabla_k = \begin{bmatrix} \partial_s \\ \frac{ik}{s} \\ \partial_z \end{bmatrix}, \quad \nabla_{k^{\cdot}} = \left[\partial_s + \frac{1}{s}, \frac{ik}{s}, \partial_z\right], \quad \Delta_k = \begin{bmatrix} \nabla_k^2 - \frac{1}{s^2} & -\frac{2ik}{s^2} & 0 \\ \frac{2ik}{s^2} & \nabla_k^2 - \frac{1}{s^2} & 0 \\ 0 & 0 & \nabla_k^2 \end{bmatrix},$$

problem $\mathscr{P}^k$ can be written in the more compact form:

$$\nabla_k \cdot \tilde{\mathbf{u}}^k = 0, \tag{19a}$$

$$\partial_t \tilde{\mathbf{u}}^k + 2C\hat{\mathbf{z}} \times \tilde{\mathbf{u}}^k + \nabla_k \tilde{P}^k = \Delta_k \tilde{\mathbf{u}}^k + \tilde{\mathbf{b}}^k, \tag{19b}$$

$$\partial_t \tilde{T}^k = \frac{1}{Pr}\nabla_k^2 \tilde{T}^k + \tilde{b}_T^k. \tag{19c}$$

As the fields sought are real, each field (for instance the pressure $\tilde{P}^k$) satisfies by construction the following symmetry in Fourier space

$$\tilde{P}^k = \overline{\tilde{P}^{-k}}, \tag{20}$$

where the overbar denotes complex conjugate. Consequently, the previous system has to be solved for positive k only. We will restrict our study to nonnegative k in the remainder of this paper.

The meridional boundary conditions that $(\tilde{u}_s^k, \tilde{u}_\phi^k, \tilde{u}_z^k)$ and $\tilde{T}^k$ must satisfy on $\partial\Omega$ stem directly from the three-dimensional ones. In particular, if we assume that $\mathbf{u} = \mathbf{0}$ and $T = 0$ on $\partial\breve{\Omega}$, we require that for all k

$$\tilde{\mathbf{u}}^k = \mathbf{0} \quad \text{on } \partial\Omega, \tag{21}$$

$$\tilde{T}^k = 0 \quad \text{on } \partial\Omega. \tag{22}$$

4. Cylindrical weak form and axial conditions

The singularity of the cylindrical coordinate system imposes extra conditions to be met by the unknown fields on the axis. The determination of these axial conditions has been addressed by several authors in the past (see e.g. [42,23,43], and references therein). For the specific purpose of deriving the variational formulation associated with $\mathscr{P}^k$, we rely on the recent work by Lopez et al. [43] and Bernardi et al. [5] and introduce the distinction between essential and natural axial conditions. The latter will be automatically satisfied through the variational formulation, while the former have to be enforced for the variational problem to be well-posed. To derive the weak formulation, we follow [5] and define the inner product $(\cdot,\cdot)_1$ over the meridional domain Ω

$$(f,g)_1 = \int_\Omega \bar{f}g \, \mathrm{d}\Omega, \tag{23}$$

in which $\mathrm{d}\Omega = 2\pi s \, \mathrm{d}s \, \mathrm{d}z$. We will omit the 2π factor in the remainder of this paper without loss of generality. At this stage, it is necessary to introduce the space $L_1^2(\Omega)$ of functions w such that

$$\|w\|_1^2 = \sqrt{(w,w)_1} < +\infty. \tag{24}$$

The weighted Sobolev space H_1^1 contains functions in $L_1^2(\Omega)$ whose first order partial derivatives are also in $L_1^2(\Omega)$.

$$H_1^1(\Omega) = \left\{ w \in L_1^2(\Omega); \partial_s w \in L_1^2(\Omega), \partial_z w \in L_1^2(\Omega) \right\}. \tag{25}$$

Similarly, $\mathbf{H}_1^1(\Omega)$ is the space of vector fields whose cylindrical components are in $H_1^1(\Omega)$. We introduce as well

$$H_{1\circ}^1 = \left\{ w \in H_1^1(\Omega), w = 0 \text{ on } \partial\Omega \right\}. \tag{26}$$

After dotting Eq. (19b) with a function $\mathbf{w}$ in $\mathbf{H}_1^1(\Omega)$, and integrating over Ω, one can show that within this cylindrical framework, the gradient form a_k writes

$$a_k(\mathbf{w}, \tilde{\mathbf{u}}^k) = a_0(w_s, \tilde{u}_s^k) + a_0(w_\phi, \tilde{u}_\phi^k) + a_0(w_z, \tilde{u}_z^k) + \left(\frac{w_s}{s}, \frac{(1+k^2)\tilde{u}_s^k + 2ik\tilde{u}_\phi^k}{s} \right)_1$$

$$+ \left(\frac{w_\phi}{s}, \frac{(1+k^2)\tilde{u}_\phi^k - 2ik\tilde{u}_s^k}{s} \right)_1 + \left(\frac{w_z}{s}, \frac{k^2\tilde{u}_z^k}{s} \right)_1, \tag{27}$$

where

$$a_0(w,v) = (\partial_s w, \partial_s v)_1 + (\partial_z w, \partial_z v)_1. \tag{28}$$

As pointed out in [43], the essential axial conditions are the ones that ensure that the integrals involved in definition (27) remain finite. In other words, we have to make sure that the following conditions hold on Γ (where $s = 0$):

$$\text{if } k = 0, \quad \tilde{u}_s^k = \tilde{u}_\phi^k = 0, \tag{29a}$$

$$\text{if } k = 1, \quad \tilde{u}_s^k + \mathrm{i}k\tilde{u}_\phi^k = \tilde{u}_z^k = 0, \tag{29b}$$

$$\text{if } k > 1, \quad \tilde{u}_s^k = \tilde{u}_\phi^k = \tilde{u}_z^k = 0. \tag{29c}$$

Likewise, the scalar fields $\tilde{P}^k$ and $\tilde{T}^k$ must behave like $\tilde{u}_z^k$. Notice that condition (29b) for $k = 1$ allows for material flow through Γ. By performing a Taylor expansion of the field variables in the neighbourhood of Γ, one can show more generally that the behaviour of the velocity components next to the axis is as follows ([42], and references therein):

$$\tilde{u}_s^k \propto \alpha s^{k-1}, \tag{30}$$

$$\tilde{u}_\phi^k \propto \mathrm{i}\alpha s^{k-1}, \tag{31}$$

$$\tilde{u}_z^k \propto \beta s^k. \tag{32}$$

Consequently, as shown in a slightly different form in [43] and detailed in [5], the meridional fields are expected to satisfy a series of natural axial conditions which write

$$\partial_s^m \tilde{u}_s^k = 0, \quad m = 1, \ldots, k-2, \quad k \geqslant 3, \tag{33}$$

$$\partial_s^m \tilde{u}_\phi^k = 0, \quad m = 1, \ldots, k-2, \quad k \geqslant 3, \tag{34}$$

$$\partial_s^m \tilde{u}_z^k = 0, \quad m = 1, \ldots, k-1, \quad k \geqslant 2. \tag{35}$$

These conditions are automatically met upon discretization of the variational formulation and we do not enforce them. On the other hand, the essential conditions (29) make it necessary to introduce yet another subspace $V_{1_\circ}^1(\Omega)$ of $H_{1_\circ}^1(\Omega)$ such that

$$V_{1_\circ}^1(\Omega) = \left\{ w \in H_{1_\circ}^1(\Omega); \ w = 0 \text{ on } \Gamma \right\}. \tag{36}$$

The space of suitable velocities (resp. temperatures) $\mathbf{H}_{1_\circ}^k(\Omega)$ (resp. $H_{1_\circ}^k(\Omega)$) for a given Fourier mode k is then given by [5]

$$\mathbf{H}_{1_\circ}^k(\Omega) = \begin{cases} V_{1_\circ}^1(\Omega) \times V_{1_\circ}^1(\Omega) \times H_{1_\circ}^1(\Omega) & \text{if } k = 0, \\ \left\{ (\tilde{u}_s^k, \tilde{u}_\phi^k, \tilde{u}_z^k) \in H_{1_\circ}^1(\Omega) \times H_{1_\circ}^1(\Omega) \times V_{1_\circ}^1(\Omega); \tilde{u}_s^k + \mathrm{i}k\tilde{u}_\phi^k = 0 \text{ on } \Gamma \right\} & \text{if } k = 1, \\ V_{1_\circ}^1(\Omega) \times V_{1_\circ}^1(\Omega) \times V_{1_\circ}^1(\Omega) & \text{if } k \geqslant 2, \end{cases} \tag{37}$$

$$H_{1_\circ}^k(\Omega) = \begin{cases} H_{1_\circ}^1(\Omega) & \text{if } k = 0, \\ V_{1_\circ}^1(\Omega) & \text{if } k \geqslant 1. \end{cases} \tag{38}$$

We can now write the variational formulation $\mathscr{W}^k$ equivalent to problem $\mathscr{P}^k$ $\forall k \geqslant 0$, find $\tilde{\mathbf{u}}^k, \tilde{P}^k, \tilde{T}^k$ in $\mathbf{H}_{1_\circ}^k(\Omega) \times L_1^2(\Omega) \times H_{1_\circ}^k(\Omega)$, such that

$$\forall q \in L_1^2(\Omega), \quad -d_k(\tilde{\mathbf{u}}^k, q) = 0, \tag{39a}$$

$$\forall \mathbf{w} \in \mathbf{H}_{1_\circ}^k(\Omega), \quad (\mathbf{w}, \partial_t \tilde{\mathbf{u}}^k)_1 + 2Cc(\mathbf{w}, \tilde{\mathbf{u}}^k) - d_k(\mathbf{w}, \tilde{P}^k) + a_k(\mathbf{w}, \tilde{\mathbf{u}}^k) = (\mathbf{w}, \tilde{\mathbf{b}}^k)_1, \tag{39b}$$

$$\forall v \in H_{1_\circ}^k(\Omega), \quad (v, \partial_t \tilde{T}^k)_1 + \frac{1}{Pr} a_k(v, \tilde{T}^k) = (v, \tilde{b}_T^k)_1. \tag{39c}$$

Apart from $a_k(\mathbf{w}, \tilde{\mathbf{u}}^k)$ which we already explicited, the forms that appear here are the pressure-divergence form

$$d_k(\tilde{\mathbf{u}}, q) = \left(\partial_s \tilde{u}_s^k + \frac{1}{s} \tilde{u}_s^k + \frac{ik}{s} \tilde{u}_\phi^k + \partial_z \tilde{u}_z^k, q \right)_1, \tag{40}$$

the cylindrical Coriolis form

$$c(\mathbf{w}, \tilde{\mathbf{u}}^k) = -\left(w_s, \tilde{u}_\phi^k \right)_1 + \left(w_\phi, \tilde{u}_s^k \right)_1, \tag{41}$$

and the scalar gradient form

$$a_k(v, \tilde{T}^k) = a_0(v, \tilde{T}^k) + k^2 \left(\frac{v}{s}, \frac{\tilde{T}^k}{s} \right)_1. \tag{42}$$

In their book, Bernardi et al. [5] provide a comprehensive theoretical analysis of this problem, and give in particular the properties of the forms $a_k(\cdot, \cdot)$ and $d_k(\cdot, \cdot)$. For our practical purposes, let us emphasize that the crucial point is to approximate pressure and velocity in compatible discrete spaces. The spatial discretization is the topic of the next section.

5. Spatial discretization

5.1. Truncation of Fourier expansion

First of all, the Fourier expansions (16) are truncated to a maximum order K.

$$\{\mathbf{u}, P, T, b_T, \mathbf{b}\} = \sum_{k=-K}^{k=+K} \left\{ \tilde{\mathbf{u}}^k, \tilde{P}^k, \tilde{T}^k, \tilde{b}_T^k, \tilde{\mathbf{b}}^k \right\} e^{ik\phi}, \tag{43}$$

which, given the symmetry in complex space, leaves us with $K + 1$ meridional problems to solve.

5.2. Spectral element discretization of the meridional problems

For each Fourier mode k in $\{0,..,K\}$, each functional space $\mathbf{H}_{1\circ}^k(\Omega)$, $L_1^2(\Omega)$, $H_{1\circ}^k(\Omega)$ involved in $\mathscr{W}^k$ has to be approximated by a finite dimensional space $\mathbf{X}_{h\circ}^k(\Omega)$, $\mathbb{Y}_h(\Omega)$, $\mathbb{X}_{h\circ}(\Omega)$, respectively. We described in detail the spatial discretization of $\mathscr{W}^0$ and spaces $\mathbf{X}_{h\circ}^0(\Omega)$ and $\mathbb{Y}(\Omega)$ in a previous paper dealing with the axisymmetric Navier–Stokes equation in a rotating frame [44]. In [44], after decomposing the meridional domain in a collection of spectral elements Ω_e, we expanded the field variables upon elemental tensorized bases of Lagrangian interpolants defined over the family of Gauss–Lobatto–Legendre (GLL) quadrature points. Exception was made for elements sharing an edge with Γ (termed *axial* elements): in this case, a Gauss–Lobatto–Jacobi (0,1) (GLJ01) quadrature, which incorporates the cylindrical radius in the weight, was used in the direction orthogonal to Γ (it was incorrectly referred to as a *weighted* Gauss–Lobatto–Legendre formula). For a general description of Gauss–Lobatto–Jacobi interpolation and quadrature, the reader is referred to appendices A and B of the treatise by Karniadakis and Sherwin [45].

The extra non-axisymmetric discrete spaces we are interested in here are the complexified extension of these real spaces, with the distinction that different axial conditions (29) have to be enforced depending on the wavenumber k. This is done in practice by means of a mode-dependent mask array.

5.2.1. Tiling of the meridional domain
We now provide the essential details of the meridional discretization. First of all, as illustrated in Fig. 2, the global domain Ω is decomposed into a collection of n_e non-overlapping elements Ω_e, such that:
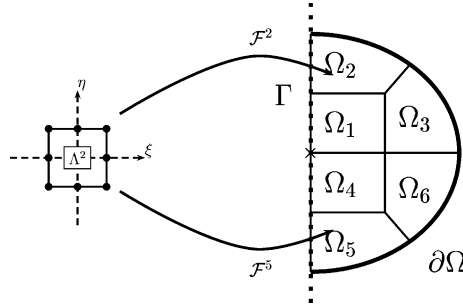
Fig. 2. Tiling of our companion meridional domain in a collection of $n_e = 6$ non-overlapping elements. Each element e is the image of a reference square (called the parent element) under an invertible mapping $\mathscr{F}^e$.

$$\bar{\Omega} = \bigcup_{e=1}^{n_e} \overline{\Omega_e}. \tag{44}$$

Here, each Ω_e is the image of a reference square $\Lambda^2 = [-1, +1]^2$ under a local invertible mapping $\mathscr{F}^e : (\xi, \eta) \in \Lambda^2 \Rightarrow (s, z) \in \overline{\Omega_e}$ with a well-defined inverse. In our current code, the mapping can be either analytical or sub-parametric, depending on the complexity of Ω. A parametric mapping is termed sub-parametric if a lower order is used to map coordinates as compared to the dependent variables, see e.g. [45]. In the case of an axial element, our conventions are such that the direction normal to Γ corresponds to the ξ direction in the parent element.

5.2.2. Discrete functional spaces and quadratures

In each spectral element Ω_e, velocity, pressure and temperature are approximated locally by means of tensorized polynomials. To avoid spurious pressure modes, Bernardi and Maday [46] suggested to discretize velocity and pressure by polynomials of different order, in the following spaces

$$\mathbf{X}_{h\circ}^k = \mathbf{H}_{1\circ}^k(\Omega) \cap \mathbf{P}_{N,n_e}, \tag{45}$$

$$\mathbb{Y}_h = L_1^2(\Omega) \cap \mathbb{P}_{N-2,n_e}, \tag{46}$$

where

$$\mathbb{P}_{N,n_e} = \left\{ w(\mathscr{F}^e(\xi,\eta))|_{\Omega_e} \in P_N(\xi) \times P_N(\eta), e = 1, n_e \right\} \tag{47}$$

and

$$\mathbf{P}_{N,n_e} = \mathbb{P}_{N,n_e} \times \mathbb{P}_{N,n_e} \times \mathbb{P}_{N,n_e}. \tag{48}$$

Here, P_N is the space of those polynomials defined over $[-1,1]$ of degree less or equal to N. It can been shown that the lower degree used to discretize pressure in this so-called $P_N - P_{N-2}$ approach provides a unique solution to the problem of interest [47].

Likewise, to discretize the temperature field, we choose

$$\mathbb{X}_{h\circ}^k = H_{1\circ}^k(\Omega) \cap \mathbb{P}_{N,n_e}. \tag{49}$$

We follow a Galerkin approach and choose velocity and temperature trial functions in the same spaces. Each integral involved in $\mathscr{W}^k$ is broken into a sum of elemental integrals which are in turn computed in the reference square Λ^2. For instance, the integral of an arbitrary function g over Ω is written as

$$\int_\Omega g(s,z)s \, \mathrm{d}s \, \mathrm{d}z = \sum_{e=1}^{n_e} \int_{\Omega_e} g(s,z)s \, \mathrm{d}s \, \mathrm{d}z = \sum_{e=1}^{n_e} \int_{\Lambda^2} g(\mathscr{F}^e(\xi,\eta))s^e(\xi,\eta)|\mathscr{J}^e|(\xi,\eta)\mathrm{d}\xi \, \mathrm{d}\eta, \tag{50}$$

where $|\mathscr{J}^e|$ is the Jacobian of the mapping. From there, the procedure we apply to compute each elemental integral is standard, and is described in detail in [44].

If Ω_e is not axial, variables are expanded on Gauss–Lobatto–Legendre (GLL) Lagrangian interpolants, in conjunction with a GLL quadrature formula of order N, the nodes and weights of which we denote by ξ_i and ρ_i, respectively. Pressure is expanded on the Lagrangian interpolants defined by the inner GLL nodes only. If Ω_e is axial, GLJ01 Lagrangian bases are used in the direction orthogonal to Γ (ξ in our conventions), along with a GLJ01 quadrature, the nodes and weights of which we now denote by ζ_i and σ_i, respectively. GLL bases and quadrature are used in the η-direction. A description of GLL and GLJ01 quadratures can be found in [5, chapter 4] and [45, Appendices A and B]. Pressure is expanded on the Lagrangian bases defined by the tensorization of the inner GLJ01 nodes in the ξ direction with the inner GLL nodes in the η direction.

An example of a meridional mesh is shown in Fig. 3. Each elemental subgrid contains $(N+1)^2$ degrees of freedom for each cylindrical component of velocity and for temperature, and $(N-1)^2$ pressure degrees of freedom. There exists grid points on Γ, which is crucial in order to enforce the essential axial conditions (29a).

5.2.3. Implementation – boundary and axial conditions

As pointed out by Deville et al. [48], the use of Lagrangian bases enables one to enforce the continuity of the velocity and temperature fields simply by equating coincident nodal values (in the geometrically conforming case). This is practically done by introducing the connectivity matrix Q which maps a global field
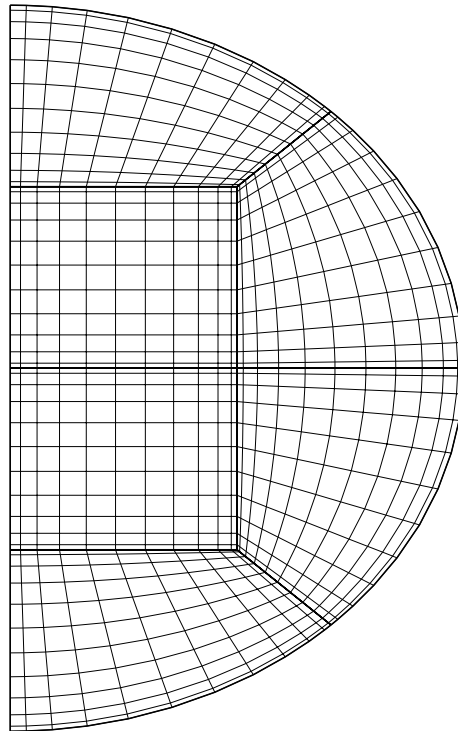

Fig. 3. Meridional SEM grid, comprising 6 elements of polynomial order 10. Aside from the standard clustering of grid points near the elements edges, note the asymmetry in the positions of grid points in the s direction for elements in contact with Γ. This follows from the application of the Gauss–Lobatto–Jacobi quadrature (0,1) rule in this direction.

F into a collection of local (elemental) fields F^e. Its transposed, Q^T is used to sum up values for interfaces nodes, leaving the interior values unchanged, see e.g. [48, Section 4.5.1].

In practice, data are stored locally and most of the operations are done at a local level. In particular, our implementation permits the decomposition of the meridional domain Ω in subdomains (containing a small number of spectral elements), which can be assigned to different processors. We retained this strategy as opposed to distributing the various $k = 0, 1, 2, \ldots, K$ meridional problems among different processors in order to get a work load as equally balanced as possible between processors. Tomboulides [42] assigned one meridional problem to each processor and he observed in his calculations that the axisymmetric solves were substantially more time consuming than the non-axisymmetric ones, which resulted in an important latency.

As an example, let us pick two fields in $H_1^1(\Omega)$, v and w, and see how their inner product is implemented. Let V and W be the global vectors of their nodal values and let V_{ij}^e and W_{ij}^e denote their nodal values at node (i,j) inside each element Ω_e. Their inner product $(\cdot,\cdot)_1$ writes

$$(v,w)_1 = \int_\Omega \bar{v}ws \, \mathrm{d}s \, \mathrm{d}z = \sum_{e=1}^{n_e} \int_{\Omega_e} \bar{v}ws \, \mathrm{d}s \, \mathrm{d}z = \sum_{e=1}^{n_e} (\bar{V}^e)^T M^e W^e, \tag{51}$$

or, equivalently, $= \bar{V}^T Q^T M Q W.$ (52)

in which M is the block-diagonal mass matrix comprising local (diagonal) mass matrices M^e

$$M_{iji'j'}^e = \delta_{ii'}\delta_{jj'} \times \begin{cases} \sigma_i \rho_j \frac{s_{ij}^e}{1+\zeta_i}|\mathscr{J}_{ij}^e| & \text{if } \Omega_e \text{ is axial,} \\ \rho_i \rho_j s_{ij}^e |\mathscr{J}_{ij}^e| & \text{otherwise,} \end{cases} \tag{53}$$

where $s_{ij}^e = s^e(\mathscr{F}^e(\xi_i,\xi_j))$ (resp. $s^e(\mathscr{F}^e(\zeta_i,\xi_j)z)$) and $|\mathscr{J}_{ij}^e| = |\mathscr{J}^e|(\mathscr{F}^e(\xi_i,\xi_j))$ (resp. $|\mathscr{J}_{ij}^e| = |\mathscr{J}^e|(\mathscr{F}^e(\zeta_i,\xi_j))$) in the non-axial (resp. axial) case. The assembled matrix $Q^T M Q$ is never formed as such. Instead, its action on a vector is computed at the elemental level and the operation QQ^T, referred to as the direct stiffness summation [49,48], is performed to obtain ultimately a local field of elemental nodal variables. In the case of a parallel calculation, applying QQ^T requires inter-processors communications. These are handled according to the message passing paradigm [50].

As an aside, note that the apparent singularity in the expression of the mass matrix in the axial case for $\zeta_0 = -1$ (or equivalently when $s = 0$) can be removed by application of L'Hospital rule.

Dirichlet and essential axial boundary conditions are enforced at the elemental level by means of a mask array, which acts on the three components of velocity as well as on temperature. It depends in each case on the Fourier mode considered. This mask array is essentially a diagonal matrix of coefficient one everywhere, save for these nodes which belong to $\overline{\Omega_e} \cap \partial\Omega$ (and depending on the value of k, on $\overline{\Omega_e} \cap \Gamma$), in which case the entry is zero. The mask $\mathscr{T}_k^e$ applied to the temperature field is always diagonal. The only case for which the velocity mask $\mathscr{V}_k^e$ is not diagonal corresponds to $k = 1$, for which the condition $\tilde{u}_s^1 + ik\cup^1 = 0$ has to be enforced on Γ.

For instance, enforcing the boundary and axial conditions for temperature requires to replace M^e by $\mathscr{T}_k^e M^e \mathscr{T}_k^e$ in (51), or, equivalently, if $\mathscr{T}_k$ denotes the block diagonal matrix made of elementary bricks $\mathscr{T}_k^e$, M by $\mathscr{T}_k M \mathscr{T}_k$ in (52). The same logic applies to the other matrices involved the semi-discrete form of $\mathscr{W}^k$.

5.2.4. Semi-discrete problem

Even if most of the operations are done at the elemental level, we will retain for clarity in this paragraph a global notation: in what follows U^k, P^k, T^k, B^k, and T^k are the vectors of nodal values associated with velocity, pressure, temperature, and the right-hand side forcing terms.

The semi-discrete problem writes for a given mode k: Find U^k, P^k, T^k such that

$$-\mathsf{D}_k \mathscr{V}_k \mathbf{Q} \mathsf{U}^k = 0, \tag{54a}$$

$$\mathbf{M}_k \frac{\mathrm{d}\mathsf{U}^k}{\mathrm{d}t} + 2C\mathbf{C}_k \mathsf{U}^k - \mathbf{Q}^{\mathrm{T}} \overline{\mathscr{V}}_k^{\mathrm{T}} \bar{\mathsf{D}}_k^{\mathrm{T}} \mathsf{P}^k + \mathbf{K}_k \mathsf{U}^k = \mathbf{Q}^{\mathrm{T}} \bar{\mathscr{V}}_k^{\mathrm{T}} \mathbf{M} \mathsf{B}^k, \tag{54b}$$

$$M_k \frac{\mathrm{d}\mathsf{T}^k}{\mathrm{d}t} + \frac{1}{Pr} K_k \mathsf{T}^k = Q^{\mathrm{T}} \mathscr{T}_k M \mathsf{T}^k. \tag{54c}$$

In this set, $\mathbf{Q}$ denotes the vectorial extension of the connectivity matrix and $\mathbf{M}$ is the vectorial extension of the unassembled mass matrix M defined above. $\mathbf{M}_k = \mathbf{Q}^{\mathrm{T}} \bar{\mathscr{V}}_k^{\mathrm{T}} \mathbf{M} \mathscr{V}_k \mathbf{Q}$ and $M_k = Q^{\mathrm{T}} \mathscr{T}_k M \mathscr{T}_k Q$ are the velocity and temperature mass matrices consistent with the boundary conditions. Background rotation appears through the antisymmetric Coriolis matrix

$$\mathbf{C}_k = \begin{bmatrix} 0 & -\mathbf{M}_k & 0 \\ \mathbf{M}_k & 0 & 0 \\ 0 & 0 & 0 \end{bmatrix}, \tag{55}$$

D_k is the (rectangular) divergence matrix and $\bar{\mathsf{D}}_k^{\mathrm{T}}$ is the associated gradient matrix. The scalar stiffness matrix K_k is given by $Q^{\mathrm{T}} \mathscr{T}_k K_k^{\mathrm{B}} \mathscr{T}_k Q$ in which K_k^{B} is the block matrix comprising the elemental stiffness matrices K_k^e. The vectorial stiffness matrix $\mathbf{K}_k$ is likewise given by $\mathbf{Q}^{\mathrm{T}} \bar{\mathscr{V}}_k^{\mathrm{T}} \mathbf{K}_k^{\mathrm{B}} \mathscr{V}_k \mathbf{Q}$, where, again, $\mathbf{K}_k^{\mathrm{B}}$ is the block matrix built from the elemental bricks $\mathbf{K}_k^e$. We provide extra details on the actual implementation of K_k^e and $\mathbf{K}_k^e$ in Appendix A, and in particular on how the singularity due to forms of the kind $(\frac{w}{s}, \frac{v}{s})_1$ in Eqs. (27) and (42) is handled.

6. Temporal discretization

The temporal discretization we apply to Eqs. (54a) relies on earlier SEM studies of the Navier–Stokes equations [51] and recent SEM oceanic and atmospheric circulations models [52,34,53,38], as well on the treatise by Deville et al. [48].

The temperature solve is decoupled from the velocity–pressure solve. The coupled velocity–pressure problem is handled following a consistent decoupling strategy applied at the discrete level, resulting in an overall second-order temporal accuracy.

6.1. Timemarching

Let Δt be the timestep and U_n^k, P_n^k, T_n^k, B_n^k, and T_n^k denote the values of U^k, P^k, T^k, B^k, and T^k at the discrete time $t_n = n\Delta t$. Time derivatives are approximated by a second-order backward differentiation formula of order 2 (BDF2), which is unconditionally stable. This gives

$$\frac{\mathrm{d}\{\mathsf{U}^k, \mathsf{T}^k\}}{\mathrm{d}t} \bigg|_{n+1} \approx \frac{3\{\mathsf{U}_{n+1}^k, \mathsf{T}_{n+1}^k\} - 4\{\mathsf{U}_n^k, \mathsf{T}_n^k\} + \{\mathsf{U}_{n-1}^k, \mathsf{T}_{n-1}^k\}}{2\Delta t}. \tag{56}$$

Nonlinear right-hand side forcing terms are approximated by means of a third-order Adams–Bashforth formula (AB3) [48]:

$$\{\mathsf{B}_{n+1}^k, \mathsf{T}_{n+1}^k\} \approx \frac{23}{12}\{\mathsf{B}_n^k, \mathsf{T}_n^k\} - \frac{4}{3}\{\mathsf{B}_{n-1}^k, \mathsf{T}_{n-1}^k\} + \frac{5}{12}\{\mathsf{B}_{n-2}^k, \mathsf{T}_{n-2}^k\}. \tag{57}$$

In practice, B^k and T^k contain quadratic terms which couple Fourier modes. They are computed in the physical domain and then transformed back into Fourier space by means of a fast Fourier transform algorithm [54]. As we perform the domain decomposition in the meridional plane, this procedure is local and does not require inter-processors communications. The explicit AB3 formula causes the timestep to be limited to a value proportional to the minimum grid spacing h:

$$\Delta t < Ch/U, \tag{58}$$

in which C is an order 1 constant and U is the maximal pointwise velocity. For an axisymmetric problem, h is equal to h_{med}, the minimal grid-spacing in the meridional plane. The clustering of grid points near elemental boundaries is such that $h_{\text{med}} \propto 1/(n_e \ _{\text{N}}^2)$. For a 3D problem, using the equidistant Fourier grid in the azimuthal direction, we have observed that h is typically equal to a fraction of h_{med}, due to the clustering of points near Γ. We will address issues related to the pole problem in the discussion.

The linear viscous and Coriolis operators in Eqs. (54b) and (54c) are treated implicitly, and the pressure field P_{n+1}^k is written as

$$P_{n+1}^k = P_n^k + \delta P^k, \tag{59}$$

where δP^k is the pressure increment to be computed.

After applying these different formulas, one ends up with the following problem to solve at each time step

$$\mathbf{A}_k U_{n+1}^k - \mathbf{Q}^{\text{T}} \bar{\mathscr{V}}_k^{\text{T}} \bar{D}_k^{\text{T}} \delta P^k = F_{n+1}^k, \tag{60}$$

$$-D_k \mathscr{V}_k \mathbf{Q} U_{n+1}^k = 0, \tag{61}$$

$$A_k T_{n+1}^k = F_{Tn+1}^k, \tag{62}$$

in which $\mathbf{A}_k$ is a modified vectorial Helmholtz operator

$$\mathbf{A}_k = a_i \Delta t^{-1} \mathbf{M}_k + 2 a_c C \mathbf{C}_k + a_v \mathbf{K}_k, \tag{63}$$

in which $(a_i, a_c, a_v) = (3/2, 1, 1)$. The right hand side forcing term writes

$$F_{n+1}^k = \mathbf{Q}^{\text{T}} \bar{\mathscr{V}}_k^{\text{T}} (\mathbf{M} B_{n+1}^k + \bar{D}_k^{\text{T}} P_n^k) + \mathbf{M}_k \Delta t^{-1} (2 U_n^k - \frac{1}{2} U_{n-1}^k). \tag{64}$$

The symmetric scalar Helmholtz operator A_k has the form

$$A_k = a_i \Delta t^{-1} M_k + a_v Pr^{-1} K_k, \tag{65}$$

and the right hand side forcing term F_{Tn+1}^k writes

$$F_{Tn+1}^k = Q^{\text{T}} \mathscr{T}_k M B_{Tn+1}^k + M_k \Delta t^{-1} (2 T_n^k - \frac{1}{2} T_{n-1}^k). \tag{66}$$

6.2. Temperature solve

To obtain the value of the temperature at the next time step, we solve Eq. (62) by means of a diagonally preconditioned conjugate gradient (PCG) method. The value of Δt imposed by the stability requirements (58) resulting from the AB3 formula is indeed typically such that A_k is diagonally dominant. As the quantities involved are complex numbers (except for T^0 which is real), the real and imaginary parts of T_{n+1}^k are computed independently. This remark applies to the velocity and pressure solves introduced below.

6.3. A discrete decoupling scheme for the velocity-pressure subproblem

Turning now our attention to the modified Stokes problem involving velocity and pressure, we note that its four-dimensional character precludes a direct solve and we follow instead the decoupling strategy exposed by Fischer [51], which was based upon earlier studies by Maday et al. [55] and Couzy [56].

First of all, the so-called inhomogeneity g^k is computed, according to

$$g^k = -\mathrm{D}_k \mathscr{V}_k \mathbf{Q} \mathbf{A}_k^{-1} \mathrm{F}_{n+1}^k = -\mathrm{D}_k \mathscr{V}_k \mathbf{Q} \mathrm{U}^{k\star}, \tag{67}$$

where $\mathrm{U}^{k\star}$ can be interpreted as a first guess for the kth velocity mode, which does not satisfy the divergence-free constraint. The operator $\mathbf{A}_k$ is inverted iteratively, using a preconditioned stabilized biconjugate gradient method [57] when $C \neq 0$, and a PCG algorithm otherwise. The preconditioner used is the diagonal of $\mathbf{A}_k$, for the reasons stated above.

The estimate $\mathrm{U}^{k\star}$ is then improved through the calculation of the pressure increment $\delta \mathrm{P}^k$, which is obtained after inversion of the pseudo-Laplacian operator E_k:

$$\delta \mathrm{P}^k = E_k^{-1} g^k, \tag{68}$$

where $E_k = a_i^{-1} \Delta t \mathrm{D}_k \mathscr{V}_k \mathbf{Q} \mathbf{M}_k^{-1} \mathbf{Q}^{\mathrm{T}} \bar{\mathscr{V}}_k^{\mathrm{T}} \bar{\mathrm{D}}_k^{\mathrm{T}}$. This symmetric operator is inverted by means of a PCG algorithm. The preconditioner we use is an adaptation of the overlapping Schwarz technique presented by Fischer [51] to our cylindrical meridional problems. This refined technique is unavoidable because of the poor conditioning of the pseudo-Laplacian operator, which is defined across the spaces $\mathbf{X}_{h_\circ}^k$ and $\mathbb{Y}_h$. We developed this technique at first in the axisymmetric context [44], for which we typically found a factor of ten reduction in the iteration count in the pressure increment solve with respect to the non-preconditoned case, resulting in a threefold decrease in the CPU time cost of the pressure calculation. We observe the same behaviour with the extension of the preconditioner to non-axisymmetric Fourier modes.

Note also that the pressure operator that follows from the standard Uzawa decoupling is $\mathrm{D}_k \mathscr{V}_k \mathbf{Q} \mathbf{A}_k^{-1} \mathbf{Q}^{\mathrm{T}} \bar{\mathscr{V}}_k^{\mathrm{T}} \bar{\mathrm{D}}_k^{\mathrm{T}}$, and not the approximated E_k. Applying directly a PCG algorithm to this operator means inverting (iteratively as well!) the modified Helmholtz operator $\mathbf{A}_k$ at each iteration. This approach is computationally expensive, and the trick due to [55] is to approximate $\mathbf{A}_k^{-1}$ by the diagonal $a_i^{-1} \Delta t \mathbf{M}_k^{-1}$ operator. This approximation results in a second-order residual term, which does not deteriorate the overall second-order accuracy of the scheme [51,44].

Finally, the pressure increment is used to form the final (divergence-free) velocity field at the next time step

$$\mathrm{U}_{n+1}^k = a_i^{-1} \Delta t \mathbf{M}_k^{-1} \mathbf{Q}^{\mathrm{T}} \bar{\mathscr{V}}_k^{\mathrm{T}} \bar{\mathrm{D}}_k^{\mathrm{T}} \delta \mathrm{P}^k + \mathrm{U}^{k\star}. \tag{69}$$

This splitting strategy is similar to classical splitting techniques, such as the fractional step method [58], save that the splitting is applied on the discrete form of the equations. No additional pressure boundary conditions need to be prescribed, and no extra temporal error is introduced. It is quite common in the fractional step framework to apply (inconsistent) homogeneous Neumann boundary conditions to solve for pressure, which tend to create divergence boundary layers located near the domain boundaries [40,42,48]. At the same time, it is well-known that rapidly rotating fluids embedded in a container with rigid boundaries create sharp boundary layers that induce a secondary flow in the bulk of the domain, through an Ekman pumping/suction mechanism [2]. It is therefore necessary to prevent the existence of numerical boundary layers, even if this implies, through the inversion of E_k, a larger computational cost than the one due to a fractional step approach. Let us mention, though, that the fractional step method can be improved through a more accurate representation of the pressure boundary conditions [59,43]. The computational effort can then be dramatically reduced since a $P_N - P_N$ approach can be followed for velocity and pressure. This approach leads, however, to an inexact representation of the pressure field, owing to the presence

of spurious pressure modes. The fact that pressure will certainly be a quantity of interest in future geophysical applications of our model prompted us to adopt the $P_N - P_{N-2}$ approach, along with the splitting scheme described above.

6.4. Initialization of the algorithm

For consistency, the initialization must provide second-order accurate starting values of U_n^k and T_n^k for $n = 1$ and 2, as required by the AB3 formula, and a second-order accurate estimate of P_2^k. Starting from the initial conditions U_0^k and T_0^k, a second-order Crank–Nicolson formula is applied to every right-hand side terms of set (54) (including the nonlinear terms). The resulting set is solved iteratively until stationary (U_1^k, P_1^k, T_1^k) are obtained. This procedure is repeated to get (U_2^k, P_2^k, T_2^k) from (U_1^k, P_1^k, T_1^k). Several tests (not shown) indicate that this procedure is indeed second-order accurate.

7. Examples

7.1. Cylindrical Kovasznay flow

As pointed out by Blackburn and Sherwin [60], an analytical solution to the 3D Navier–Stokes equations in cylindrical geometry can be found from a planar solution when the latter is expressed in cylindrical coordinates. The 2D Navier–Stokes equations (in the absence of background rotation) can be written

$$\partial_x u_x + \partial_y u_y = 0, \tag{70}$$

$$\frac{\partial u_x}{\partial t} + u_x \partial_x u_x + u_y \partial_y u_x = -\partial_x p + \frac{1}{Re}(\partial_x^2 + \partial_y^2)u_x, \tag{71}$$

$$\frac{\partial u_y}{\partial t} + u_x \partial_x u_y + u_y \partial_y u_y = -\partial_y p + \frac{1}{Re}(\partial_x^2 + \partial_y^2)u_y, \tag{72}$$

where (u_x, u_y) are the Cartesian components of velocity, p is pressure and Re denotes the Reynolds number. A steady solution to the previous system is the Kovasznay flow [61] defined as

$$u_x(x,y) = 1 - \exp(\lambda x)\cos(2\pi y), \tag{73}$$

$$u_y(x,y) = \frac{\lambda}{2\pi}\exp(\lambda x)\sin(2\pi y), \tag{74}$$

$$p(x) = \frac{1}{2}(1 - \exp(2\lambda x)), \tag{75}$$

where $\lambda = Re/2 - \sqrt{Re^2/4 + 4\pi^2}$. Blackburn and Sherwin [60] suggest to map the previous solution into a cylindrical coordinates system. The solution becomes fully 3D first by rotating the solution coordinates about the Cartesian x-axis by an amount α, and by introducing an offset $-\Delta$ of the cylindrical z-axis from the Cartesian x-axis. The cylindrical solution is then

$$u_s = \frac{\lambda}{2\pi}\exp(\lambda z)\sin\left(2\pi[s\cos(\phi + \alpha) + \Delta]\right)\cos(\phi + \alpha), \tag{76}$$

$$u_\phi = -\frac{\lambda}{2\pi}\exp(\lambda z)\sin\left(2\pi[s\cos(\phi + \alpha) + \Delta]\right)\sin(\phi + \alpha), \tag{77}$$

$$u_z = 1 - \exp(\lambda z) \cos\left(2\pi[s\cos(\phi + \alpha) + \Delta]\right), \tag{78}$$

$$p = \frac{1}{2}(1 - \exp(2\lambda z)). \tag{79}$$

In the remainder of this paragraph, we follow Blackburn and Sherwin [60] and take $Re = 40$, $\Delta = 0.1$ and $\alpha = 0.75$, which ensures that flow crosses the axis and that all axial terms are exercised, for real and imaginary parts of all non-axisymmetric modes. The meridional domain Ω is the $[0,0.5] \times [-0.5,1]$ rectangle. It is decomposed into four spectral elements, as illustrated in Fig. 4(a), where the mesh obtained by choosing $N = 11$ is displayed. Solutions are computed starting from the exact solution above (hereafter referred to as $\mathbf{u}_a$), and letting the numerical approximation $\mathbf{u}_h$ evolve in time until it becomes steady. The velocity boundary conditions prescribed during the evolution correspond to the value of $\mathbf{u}_a$ on the boundary nodes. The timestep is set to $\Delta t = 2 \times 10^{-3}$, which ensures that temporal errors are negligible. The maximum pointwise deviation is evaluated when steady state is reached, for the three components of velocity. To test the convergence properties of the $P_N - P_{N-2}$ spectral element approximation, the truncation K in the Fourier domain is set to 23. Shown in Fig. 4(b) is the maximum pointwise error for the axial component of velocity, $\|u_{z,h} - u_{a,h}\|_\infty$, as a function of polynomial order N (the results obtained for the equatorial components follow the same trend). The convergence to the exact solution is exponential, and the error reaches the numerical noise for $N = 13$. For completeness, we show the same type of curve fixing N to 11 and varying the truncation K in Fig. 4(c): not surprisingly, the convergence in Fourier space is also spectral – the $N = 11$ spectral element error level is obtained for $K = 17$.

The spectral convergence of the $P_N - P_{N-2}$ spectral element approximation is to our knowledge the first of the kind exposed for a fully nonlinear problem which has flow crossing the axis. In their paper, Blackburn and Sherwin [60] show a similar behaviour for the same problem, following a $P_N - P_N$ formulation, which employs GLL quadrature everywhere. They stress the need for a careful inspection of the right-hand side terms in the Poisson equation that controls the value of pressure. In particular, they show (Appendix A) that the negligent use of a Gauss–Lobatto–Jacobi $(0,1)$ quadrature can degrade the convergence from spectral to algebraic. We do not detect this degradation here, benefiting from the $P_N - P_{N-2}$ approach in conjunction with the discrete time splitting described in the previous section.
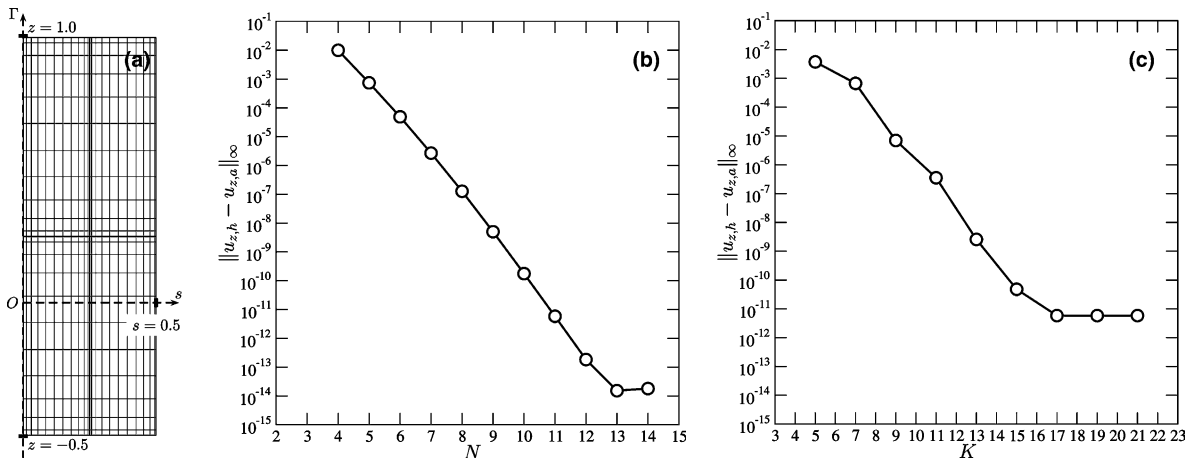

Fig. 4. (a) Spectral element grid used to calculate the cylindrical Kovasznay flow, shown here for $N = 11$. Note that the 2 elements touching the axis Γ resort to a Gauss–Lobatto–Jacobi $(0,1)$ quadrature in the radial direction. (b) Spectral element approximation convergence results for the axial component of velocity (logarithmic scale). The maximum azimuthal wavenumber K is constant and set to $K = 23$. (c) Fourier approximation convergence results for the axial component of velocity. The polynomial order N is constant and set to 11.

7.2. Thermal convection in a rotating spherical shell

Over the past decade, much has been learned on dynamo action through the numerical simulations of convection-driven magnetohydrodynamic dynamos in rotating spherical shells; see [62–64] for recent reviews. Recently, in an attempt to increase the confidence in existing codes and to provide a well-established standard solution for codes being developed, Christensen et al. [10] proposed a numerical dynamo benchmark calculation.

The first case of this benchmark is purely hydrodynamic (no magnetic effect at all) and provides an interesting and challenging test for our code. In a spherical shell $\breve{\Omega}$ of inner radius r_i and outer radius r_o, temperature is fixed to T_o and $T_o + \Delta T$ on the outer and inner boundaries, respectively. The equations are scaled with $D = r_o - r_i$ as the fundamental length scale, which makes the dimensionless radii equal to $r_o = 20/13$ and $r_i = 7/13$. The choice of scales is the same as the one exposed in Section 2 and leads to the following set of dimensionless equations:

$$\nabla \cdot \mathbf{u} = 0, \tag{80a}$$

$$Ek\left(\partial_t \mathbf{u} + \mathbf{u} \cdot \nabla \mathbf{u} - \nabla^2 \mathbf{u}\right) + 2\hat{\mathbf{z}} \times \mathbf{u} = -\nabla P + R\frac{\hat{\mathbf{r}}}{r_o}T, \tag{80b}$$

$$\partial_t T + \mathbf{u} \cdot \nabla T = \frac{1}{Pr}\nabla^2 T - \mathbf{u} \cdot \nabla T_s. \tag{80c}$$

Non-dimensional control parameters are the (modified) Rayleigh number

$$R = \frac{\alpha g_o \Delta T D}{\nu \omega}, \tag{81}$$

where α is the coefficient of thermal expansivity and g_o is gravity at the outer radius, and the Ekman and Prandtl numbers. The values used in the benchmarks are $R = 100$, $Ek = 10^{-3}$ (or, equivalently, $C = 10^3$), and $Pr = 1$. The static, radial temperature profile T_s is given by

$$T_s(r) = \frac{r_o r_i}{r} - r_i. \tag{82}$$

Furthermore, no-slip boundary conditions are used and velocity must vanish on the rigid boundaries. Initial conditions consist of a zero velocity field and of a temperature perturbation of degree and order four:

$$T(r, \theta, \phi; t = 0) = \frac{21}{\sqrt{17920\pi}}(1 - 3x^2 + 3x^4 - x^6)\sin^4\theta \cos 4\phi, \tag{83}$$

where $x = 2r - r_i - r_o$.

A quasi-stationary solution is reached within approximately 1 time unit, and Christensen et al. [10] express it by a vector function of the form

$$(\mathbf{u}, P, T) = f(r, \theta, \phi - \omega_d t), \tag{84}$$

in which ω_d is the drift frequency.

The solution is symmetric about the equator and has fourfold symmetry in longitude. Fig. 5 shows two slices representing the temperature field (left) and the velocity and pressure fields (right) at the equator. As the solution is symmetric about the equator, results exposed in what follows correspond to FSEM calculations performed in the upper part of the shell only. Moreover, the fourfold symmetry in longitude leads to a reduction of the cost of the calculation by another factor of four. Fig. 6 shows an example of a mesh used to compute this rotating Rayleigh–Bénard flow. It consists of four spectral elements of order 14 coupled with $K + 1 = 32$ Fourier modes in longitude ϕ. For this problem, nonlinear terms are computed
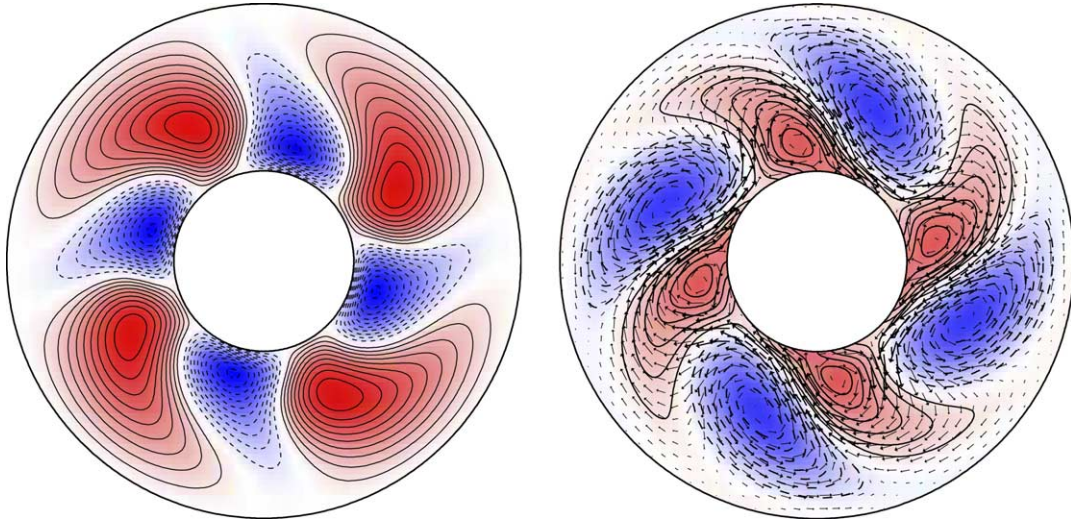
Fig. 5. Equatorial slices showing the temperature field (left) and the velocity and pressure fields (right) for the rotating convection calculation. Left: Solid lines and red regions correspond to positive temperature anomalies; dashed lines and blue regions correspond to negative temperature anomalies. Right: Solid lines (red regions) represent pressure highs; dashed lines (blue regions) represent pressure lows. Pressure highs (resp. lows) are associated with anticyclonic (resp. cyclonic) motions. (For interpretation of the references to colour in this figure the reader is referred to the web version of this article.)
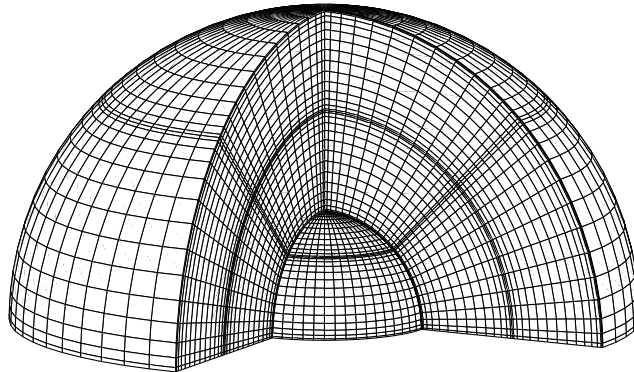
Fig. 6. Example of a Fourier-spectral element mesh used to compute the rotating Rayleigh–Bénard flow. It consists of four spectral elements of order $N = 14$ in the (s,z) meridional plane coupled with $K + 1 = 32$ Fourier modes in longitude ϕ. Nonlinear terms in ϕ are computed pseudo-spectrally on a grid of 64 points in longitude.

pseudo-spectrally on a grid of $2(K + 1)$ points in longitude and no dealiasing procedure, such as the 2/3 rule [65], was necessary for this calculation.

All original contributors to the benchmark used a spherical harmonic representation of the field varia-bles in the horizonthal (θ, ϕ) plane, along with some form of discretization in the radial direction – finite differences (FD) or Chebyshev polynomials. Further details on methods used by contributors can be found in [10].

Contributors had to provide global averages as well as local data for the quasi-steady state. The former are the mean kinetic energy e_{kin} and the value of the drift frequency ω_{d}. The latter include the value of the total temperature T_{tot} (sum of the static temperature and the temperature perturbation) and the azimuthal

velocity u_ϕ at a point $\mathbf{x}_0$ at mid-depth ($r = (r_i + r_o)/2$) in the equatorial plane ($\theta = \pi/2$), the longitude of which is given by the conditions $u_r = 0$ and $\partial_\pi u_r > 0$.

Results are plotted in Fig. 7, as a function of the spatial resolution, defined as the third root of the number of degrees of freedom for each scalar variable. We used Table 1 of Christensen et al. [10] to plot contributors' results, and superimposed results obtained via the FSEM, which are also listed in Table 1, along with the standard values suggested by Christensen et al. [10].
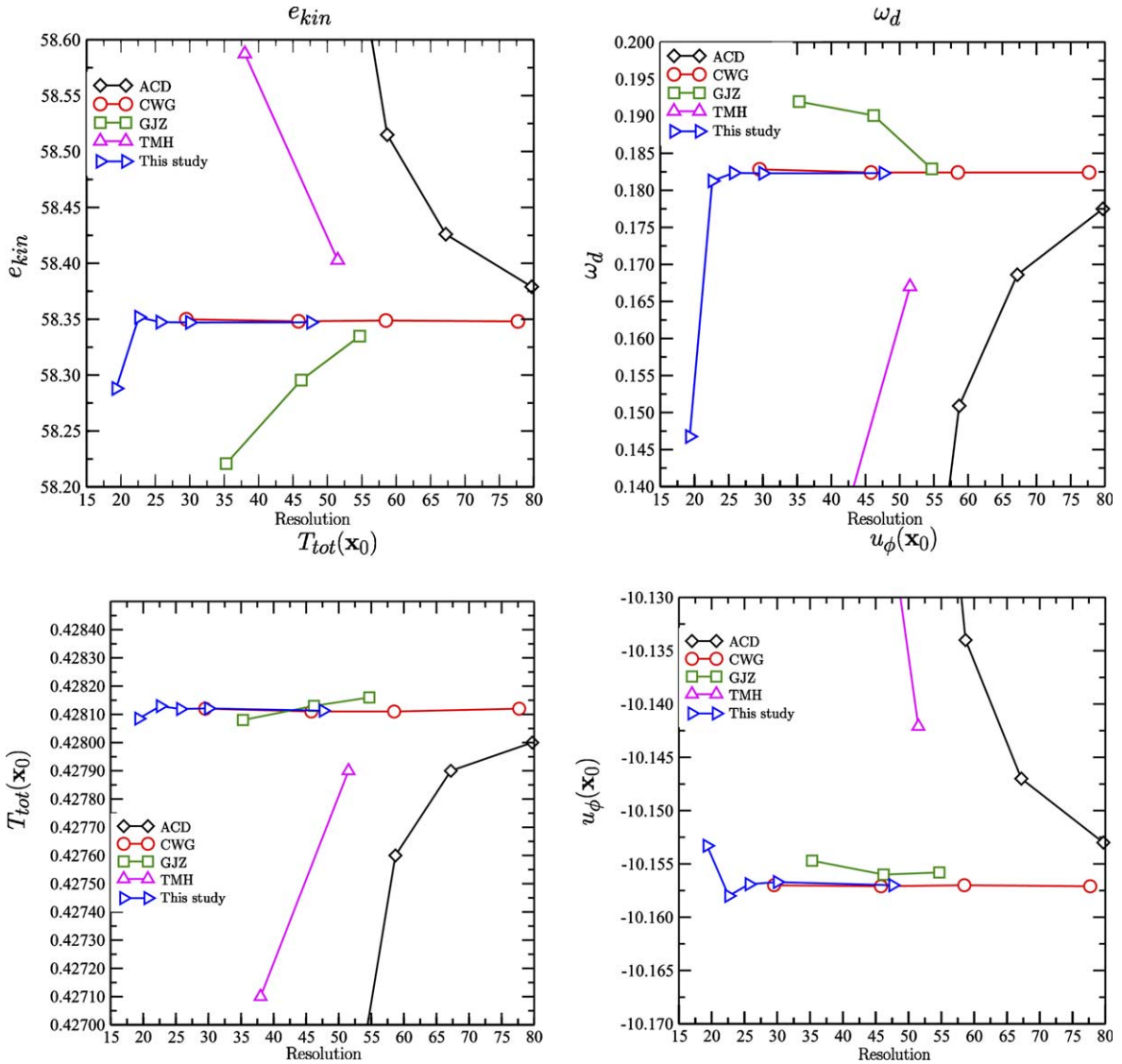

Fig. 7. Convergence of results for rotating convection calculation. Results for groups ACD, CWG, GJZ, and TMH plotted after Table 1 of [10]. For details on the methods used by these groups, see references in [10]. Results obtained by the FSEM in blue, with right triangles. Global data on top row: mean kinetic energy e_{kin} (left) and drift frequency ω_d (right). Local data on bottom row: total temperature T_{tot} (left) and azimuthal velocity u_ϕ (right). Resolution is defined as the third root of the number of degrees of freedom for each scalar variable. (For interpretation of the references to colour in this figure the reader is referred to the web version of this article.)

Table 1
Summary of results for case 0 of numerical dynamo benchmark

n_e	N	K	Resolution	e_{kin}	ω_{d}	$T_{\text{tot}}(\mathbf{x}_0)$	$u_\phi(\mathbf{x}_0)$
1	14	31	19.3	58.2880	0.14676	0.42809	−10.1533
1	18	31	22.6	58.3518	0.18127	0.42813	−10.1580
1	22	31	25.7	58.3474	0.18235	0.42812	−10.1569
4*	14	31	30.0	58.3471	0.18230	0.42812	−10.1567
4	18	63	47.6	58.3472	0.18232	0.42811	−10.1570
Standard solution [10]:				58.348	0.1824	0.42812	−10.1571
Uncertainties:				0.05	0.005	0.00012	0.002

The last two lines indicate the standard solution to this problem, as defined in [10], along with the associated error limits. n_e is the number of elements used in the meridional plane, N is the polynomial order of the Legendre approximation, and K is the maximum wave number used in the ϕ direction. Due to the equatorial symmetry, calculations are performed in the upper (northern) part of the shell only. The star indicates that results on this row were obtained using the mesh shown in Fig. 6.

Christensen et al. [10] pointed out that the different results obtained by the contributors converge to the same values within better than 2%. The rate of convergence being fast in the spectral (Chebyshev) case, and slow when finite differencing is used in the radial direction.

Table 1 shows that the results obtained with the FSEM are in excellent agreement with the suggested values (to within better than 0.05% in all cases). As seen in Fig. 7, the rate of convergence is also very satisfactory, and the FSEM is in this respect equivalent to the Chebyshev-$\mathscr{Y}_l^m$ approach. The smooth character of the sought solution prompted us to obtain finer resolutions by increasing the polynomial order N to large values and by keeping the total number of elements n_e very small. We benefited therefore from the clustering of GLL points near the boundaries and the associated good resolution of the Ekman boundary layers. In more chaotic, time-dependent situations, timestepping issues could however lead us to keep the polynomial order low (typically between 6 and 12) and to increase n_e to obtain finer resolutions.

8. Discussion – conclusion

We have presented a Fourier-spectral element model of thermal convection for a fluid filling an axisymmetric container, in a rapidly rotating reference frame. This model, which relies heavily on the recent theoretical work of Bernardi et al. [5], is based upon a Fourier expansion of the field variables in the periodic direction, and the resolution of the associated meridional problems via the spectral element method. A Gauss–Lobatto–Jacobi (0,1) quadrature is introduced to treat those elements sharing an edge with the axis of symmetry of the three-dimensional domain. Inside a meridional element, velocity and temperature are approximated by polynomials of order N in each direction of space, and a slightly lower order $(N-2)$ is used to discretize pressure. The resulting semi-discrete system is timestepped using a second-order scheme, which treats both the Coriolis and viscous terms implicitly.

Two examples have illustrated the accuracy of this approach. The first one (Section 7.1), which ignored rotation and the heat equation, was a Navier–Stokes test case taken from a recent paper by Blackburn and Sherwin [60]: this cylindrical Kovasznay flow served to illustrate the spectral convergence properties of the FSEM in a fully nonlinear setting, with flow crossing the axis (i.e. with energy in the $k = 1$ mode). These results imply that all the singularities that arise in the cylindrical expressions of the Navier–Stokes system are properly taken care of. In particular, the discrete decoupling strategy presented in Section 6 guarantees that the convergence remains spectral and does not degenerate into algebraic, as could be the case if a GLJ01 quadrature was used in a $P_N - P_N$ context [60].

Turning to geophysical considerations (Section 7.2), we then studied the rotating Rayleigh–Bénard benchmark case in a spherical shell by Christensen et al. [10]. This problem combined all the ingredients of the governing Eqs. (5a) and the smoothness of the sought solution prompted us to use a minimal n_e and large N to reproduce the reference solution with an excellent agreement.

The previous enthusiastic remarks praising spectral vs. algebraic convergence have to be confronted with practical considerations: when dealing with a nonlinear, unsteady problem (highly supercritical convection for instance), a high enough resolution is needed, which has a drastic influence on the timestep size Δt. The explicit treatment of nonlinearities implies indeed that Δt cannot exceed a value which is proportional to the smallest distance h between two grid points. In our case, the clustering of the GLL and GLJ01 points near the element boundaries is such that the meridional minimal grid spacing h_{med} is proportional to $1/(n_e N^2)$. Fig. 8 shows the minimal grid spacing h_{med} for the mesh of Fig. 6 (consisting of four spectral elements) for different values of N, along with the overall h that results from the use of a Fourier grid of 64 equidistant points in longitude. We observe that in this case $h_{\mathrm{med}} \approx 5.70h$.

This follows from the clustering of points in the polar regions, which is the root of the so-called pole problem [23, Section 18.10]. This might not be so crucial for our purposes, since calculations at large C for which this model is ultimately aimed require to resolve very thin Ekman boundary layers in the meridional plane. For larger and larger Coriolis numbers, the increase in meridional resolution is likely to outweigh the increase in K, and therefore h_{med} should be closer to h. In a strongly nonlinear context, one should anyhow use a constant (moderate) value of N (on the order of 10) and refine the resolution by increasing n_e, which allows for the model to be run on more processors. As far as performances are concerned, let us stress that the current version of the code has yet to be optimized (at the serial and parallel levels), following for instance the precepts of Deville et al. [48, chapter 8]. This task has been recently initiated, now that the model is anchored on robust (accurate) foundations. In particular, we wish to develop a new preconditioner for the modified Helmholtz operator (63) which, unlike the diagonal preconditioner, does not restrict the timestep to a fraction of C^{-1} (a fraction of ω^{-1} if one restores dimensions).

The FSEM has an overall complexity of $\mathcal{O}(Kn_e N^3)$, and a complexity per processor of $\mathcal{O}(Kn_e N^3/n_p)$, if n_p denotes the number of processors. It is fundamental to obtain good scaling performances and even more
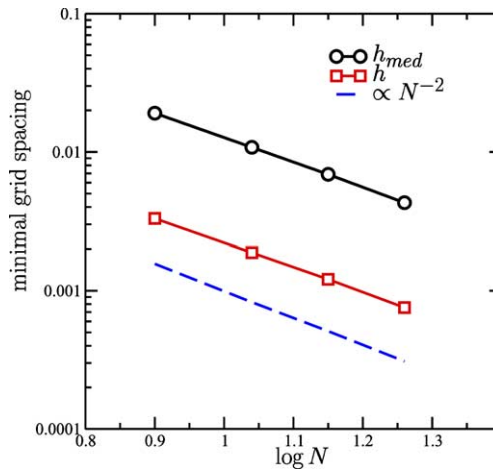

Fig. 8. Minimal grid spacing h for a three-dimensional mesh of the northern hemisphere of a spherical shell consisting of four spectral elements of varying polynomial order N. The Fourier grid has 64 equally spaced points in longitude. Also indicated is the minimal grid spacing in the meridional plane h_{med}. Both decrease as N^{-2}, as indicated by the dashed line, and are proportional: $h_{\mathrm{med}} \approx 5.70h$. Note that the points for $N = 14$ ($\log N \approx 1.15$) correspond to the mesh depicted in Fig. 6.

efficient solvers for this approach to allow to tackle challenging problems in planetary dynamics. An already very positive news in this respect is that the FSEM does not require a lot of memory, thanks to the problem reduction in longitude and the tensorized formulation, which preserves us from storing large matrices.

We cannot claim at this stage that the FSEM is definitely advantageous with respect to a fully three-dimensional SEM, which is an appealing alternative to simulate the problem of interest here, especially when the number of Fourier modes becomes large. We can stress, however, that the Fourier expansion in longitude greatly simplifies the implementation because of the dimension reduction. In particular, the overlapping Schwarz method is much easier to implement in two dimensions than it is in three dimensions [39].

To conclude, let us emphasize that the excellent agreement obtained for the rapidly rotating Rayleigh–Bénard flow is the first of the kind obtained by a method which does not rely on spherical harmonics and it is truly encouraging for future planetary applications of the model. These include the study of flows driven by precession [66,16,67], for which it is particularly important to take the ellipticity of the planet into account. The Fourier-spectral element approach is well suited for this application, as the shape of the meridional domain Ω is arbitrary. Also, as stated in the introduction, another very interesting and related application lies in the modelling of the dynamo process at work for instance in the Earth's outer core. The main difference between the Navier–Stokes equation and the so-called induction equation which governs the evolution of the magnetic field lies in the boundary conditions. On the outer boundary of the region filled by the convecting metallic liquid, the magnetic field has to be connected with an exterior potential field. This connection is straightforward if one is using spherical harmonics [6] but less amenable to a local method like ours. We are currently investigating this issue.

Appendix A. Local form of stiffness matrices – singularity removal

We provide here a detailed description of the implementation of the elementary scalar and vectorial stiffness matrices K_k^e and $\mathbf{K}_k^e$. The case of an element not in contact with Γ is standard: GLL quadrature is used in the two directions of space and no singularity has to be removed. We will therefore restrict our attention on the axial element case. The local representation of a scalar field T in such an element e takes the form

$$T|_{\Omega^e}(s^e(\xi,\eta), z^e(\xi,\eta)) = \sum_{i=0}^{N} \sum_{j=0}^{N} \mathsf{T}_{ij}^e l_i^N(\xi) h_j^N(\eta), \tag{A.1}$$

where the l_i^N and h_j^N are the Lagrangian interpolants defined over the GLJ01 and GLL points of order N, respectively (we will omit the superscript N in what follows). Applying K_k^e to T^e means evaluating (see the definition of a_k in Eq. (42))

$$(K_k^e \cdot \mathsf{T}^e)_{i'j'} = (K_0^e \cdot \mathsf{T}^e)_{i'j'} + k^2 (M_s^e \cdot \mathsf{T}^e)_{i'j'}$$

where

$$(K_0^e \cdot \mathsf{T}^e)_{i'j'} = \sum_{i=0}^{N} \sum_{j=0}^{N} \mathsf{T}_{ij}^e \int_{\Omega_e} \left\{ \partial_s (l_{i'} h_{j'}) \partial_s (l_i h_j) + \partial_z (l_{i'} h_{j'}) \partial_z (l_i h_j) \right\} \mathrm{d}\Omega_e \qquad (A.2)$$

and

$$(M_s^e \cdot \mathsf{T}^e)_{i'j'} = \sum_{i=0}^{N} \sum_{j=0}^{N} \mathsf{T}_{ij}^e \int_{\Omega_e} \frac{l_{i'} h_{j'}}{s} \frac{l_i h_j}{s} \mathrm{d}\Omega_e. \qquad (A.3)$$

Each of these integrals is computed in the parent element Λ^2. For instance, the first term on the right-hand side of (A.2) gives rise to

$$\int_{\Omega_e} \partial_s (l_{i'} h_{j'}) \partial_s (l_i h_j) \mathrm{d}\Omega_e = \int_{\Lambda^2} (\partial_\eta z^e \partial_\xi - \partial_\xi z^e \partial_\eta)(l_{i'} h_{j'})(\partial_\eta z^e \partial_\xi - \partial_\xi z^e \partial_\eta)(l_i h_j) |\mathscr{J}^e|^{-1}(\xi, \eta) s^e \, \mathrm{d}\xi \, \mathrm{d}\eta$$

$$= \int_{\Lambda^2} \left(\partial_\eta z^e l_{i'}' h_{j'} - \partial_\xi z^e l_{i'} h_{j'}' \right) \left(\partial_\eta z^e l_i' h_j - \partial_\xi z^e l_i h_j' \right) |\mathscr{J}^e|^{-1}(\xi, \eta) s^e \, \mathrm{d}\xi \, \mathrm{d}\eta. \qquad (A.4)$$

Each of the four terms involved in this sum is computed using the quadrature rules described in paragraph (5.2.2). When developing the product in Eq. (A.4), one gets for instance a term which is

$$\int_{\Lambda^2} (\partial_\eta z^e)^2 l_{i'}' h_{j'} l_i' h_j |\mathscr{J}^e|^{-1}(\xi, \eta) s^e \, \mathrm{d}\xi \, \mathrm{d}\eta$$

$$= \sum_{p=0}^{N} \sum_{q=0}^{N} \sigma_p \rho_q l_{i'}'(\zeta_p) l_i'(\zeta_p) h_{j'}(\xi_q) h_j(\xi_q) \frac{s^e(\zeta_p, \xi_q)}{1 + \zeta_p} |\mathscr{J}^e|^{-1}(\zeta_p, \xi_q)(\partial_\eta z^e(\zeta_p, \xi_q))^2$$

$$= \rho_j \delta_{jj'} \sum_{p=0}^{N} \sigma_p l_{i'}'(\zeta_p) l_i'(\zeta_p) \frac{s^e(\zeta_p, \xi_j)}{1 + \zeta_p} |\mathscr{J}^e|^{-1}(\zeta_p, \xi_j)(\partial_\eta z^e(\zeta_p, \xi_j))^2.$$

When $p = 0$, $\sigma_0 = -1$ (or equivalently $s = 0$): the singularity in the term $\frac{s^e(\zeta_p, \xi_j)}{1 + \zeta_p}$ is removed by applying L'Hospital rule and replacing this term by $\partial_\xi s^e(\xi = -1, \eta = \xi_j)$, a quantity which is derived from the knowledge of the mapping $\mathscr{F}^e$. The same logic applies to each term in Eq. (A.4) above, and, more generally, to the second part of the right-hand side of (A.2), which we expand here for the sake of completeness:

$$\int_{\Omega_e} \partial_z (l_{i'} h_{j'}) \partial_z (l_i h_j) \mathrm{d}\Omega_e = \int_{\Lambda^2} (-\partial_\eta s^e \partial_\xi + \partial_\xi s^e \partial_\eta)(l_{i'} h_{j'})(-\partial_\eta s^e \partial_\xi + \partial_\xi s^e \partial_\eta)(l_i h_j) |\mathscr{J}^e|^{-1}(\xi, \eta) s^e \, \mathrm{d}\xi \, \mathrm{d}\eta$$

$$= \int_{\Lambda^2} \left(-\partial_\eta s^e l_{i'}' h_{j'} + \partial_\xi s^e l_{i'} h_{j'}' \right) \left(-\partial_\eta s^e l_i' h_j + \partial_\xi s^e l_i h_j' \right) |\mathscr{J}^e|^{-1}(\xi, \eta) s^e \, \mathrm{d}\xi \, \mathrm{d}\eta.$$

Expressions for the derivatives h' can be found for instance in [48, p. 462]. Expressions for the less usual derivatives l' can be found in [45, Appendix C]. Note that the actual cost of the total calculation $K_0^e \cdot \mathsf{T}^e$ goes like N^3 instead of the expected N^4 thanks to the tensorized formulation and associated partial summation technique – see for instance Boyd [23, p. 184].

Let us now turn our attention to M_s^e in Eq. (A.3), which is of interest for $k > 0$ only. The associated axial condition is that T must vanish on Γ. A mask array is therefore applied prior to the calculation of

$(M_s^e \cdot \mathsf{T}^e)_{i'j'}$ to ensure that $T_{0j}^e = 0$ for all j. For the same reason the result of this operation needs to be evaluated for $i' > 0$ only (a subsequent application of the same mask array sets the axial values to zero anyway). A straightforward development of Eq. (A.3) then leads to

$$(M_s^e \cdot \mathsf{T}^e)_{i'j'} = \rho_j \sum_{i=1}^{N} \mathsf{T}_{ij'}^e \sum_{p=0}^{N} \sigma_p \frac{l_i(\zeta_p)}{s^e(\zeta_p, \xi_{j'})} \frac{l_{i'}(\zeta_p)}{s^e(\zeta_p, \xi_{j'})} \frac{s^e(\zeta_p, \xi_{j'})}{1 + \zeta_p} |\mathscr{J}^e|(\mathscr{F}^e(\zeta_p, \xi_{j'})). \tag{A.5}$$

The result of $M_s^e \cdot \mathsf{T}^e$ is the sum of two contributions, $(M_s^e \cdot \mathsf{T}^e)^1 + (M_s^e \cdot \mathsf{T}^e)^2$. If $p \neq 0$ in (A.5), there is no singularity and one gets the first term:

$$(M_s^e \cdot \mathsf{T}^e)_{i'j'}^1 = \sigma_{i'} \rho_j \mathsf{T}_{i'j'}^e \frac{1}{1 + \zeta_{i'}} \frac{1}{s^e(\zeta_{i'}, \xi_{j'})} |\mathscr{J}^e|(\mathscr{F}^e(\zeta_{i'}, \xi_{j'})). \tag{A.6}$$

On the other hand, if $p = 0$, the application of L'Hospital rule gives rise to the second contribution which includes non-diagonal terms:

$$(M_s^e \cdot \mathsf{T}^e)_{i'j'}^2 = \sigma_0 R_{i'j'}^e \rho_j \frac{s^e(\zeta_0, \xi_{j'})}{1 + \zeta_0} |\mathscr{J}^e|(\mathscr{F}^e(\zeta_0, \xi_{j'})) \sum_{i=1}^{N} \mathsf{T}_{ij'}^e R_{ij'}^e, \tag{A.7}$$

in which $R_{ij'}^e = l_i'(\zeta_0) \frac{1+\zeta_0}{s^e(\zeta_0, \xi_{j'})}$. Again, terms of the form $\frac{s^e(\zeta_0, \xi_j)}{1+\zeta_0}$ are practically replaced in the implementation by the quantity $\partial_\xi s^e(\xi = \zeta_0, \eta = \xi_j)$ whose exact expression depends on the chosen mapping $\mathscr{F}^e$ (analytical or sub-parametric).

As far as the elementary vectorial stiffness matrix $\mathbf{K}_k^e$ is concerned, one can show that it is of the form

$$\mathbf{K}_k^e = \begin{bmatrix} K_0^e + (1+k^2)M_s^e & 2ikM_s^e & 0 \\ -2ikM_s^e & K_0^e + (1+k^2)M_s^e & 0 \\ 0 & 0 & K_k^e \end{bmatrix}, \tag{A.8}$$

and its implementation follows the lines of the scalar case detailed above.

References

[1] R. Merrill, M. McElhinny, P. McFadden, The Magnetic Field of the Earth, Academic Press, New York, 1996.
[2] H.P. Greenspan, The Theory of Rotating Fluids, second ed., Breukelen Press, Brookline, MA, 1990.
[3] F.H. Busse, Thermal instabilities in rapidly rotating systems, J. Fluid. Mech. 44 (1970) 441–460.
[4] D. Gubbins, P.H. Roberts, Magnetohydrodynamics of the Earth's core, in: J.A. Jacobs (Ed.), Geomagnetism, vol. 2, Academic Press, London, 1987.
[5] C. Bernardi, M. Dauge, Y. Maday, Spectral methods for axisymmetric domains, vol. 3 of Series in Applied Mathematics, Gauthier-Villars, Paris, 1999, Numerical algorithms and tests due to Mejdi Aza.fiez.
[6] G.A. Glatzmaier, Numerical simulations of stellar convective dynamos. I. The model and method, J. Comput. Phys. 55 (1984) 461–484.
[7] W. Kuang, J. Bloxham, Numerical modeling of magnetohydrodynamic convection in a rapidly rotating spherical shell: Weak and strong field dynamo action, J. Comput. Phys. 51 (1999) 51–81.
[8] A. Tilgner, Spectral methods for the simulation of incompressible ows in spherical shells, Int. J. Numer. Meth. Fluids 30 (1999) 713–724.
[9] R. Hollerbach, A spectral solution of the magneto-convection equations in spherical geometry, Int. J. Numer. Meth. Fluids 32 (2000) 773–797.
[10] U. Christensen, J. Aubert, P. Cardin, E. Dormy, S. Gibbons, G. Glatzmaier, E. Grote, Y. Honkura, C. Jones, M. Kono, M. Matsushima, A. Sakuraba, F. Takahashi, A. Tilgner, J. Wicht, K. Zhang, A numerical dynamo benchmark, Phys. Earth Planet. Inter. 128 (2001) 25–34.
[11] S.A. Orszag, Fourier series on spheres, Mon. Weather Rev. 102 (1974) 56–75.
[12] B.A. Alpert, V. Rokhlin, A fast algorithm for the evaluation of Legendre expansions, SIAM J. Sci. Comput. 12 (1991) 158–179.
[13] P.N. Swarztrauber, W.F. Spotz, Generalized discrete spherical harmonic transforms, J. Comput. Phys. 159 (2000) 213–230.

[14] P.N. Swartztrauber, The vector harmonic transform method for solving partial differential equations in spherical geometry, Mon. Weather Rev. 121 (1993) 3415–3437.
[15] P.J. Kostelec, D.K. Maslen, D.M. Healey Jr., D.N. Rockmore, Computational harmonic analysis for tensor fields on the two-sphere, J. Comput. Phys. 162 (2000) 514–535.
[16] S. Lorenzani, A. Tilgner, Fluid instabilities in precessing spheroidal cavities, J. Fluid. Mech. 447 (2001) 111–128.
[17] W.F. Spotz, P.N. Swarztrauber, A performance comparison of associated Legendre projections, J. Comput. Phys. 168 (2001) 339–355.
[18] T. Clune, J. Elliott, M. Miesch, J. Toomre, G. Glatzmaier, Computational aspects of a code to study rotating turbulent convection in spherical shells, Parallel Comput. 25 (1999) 361–380.
[19] A. Kageyama, K. Watanabe, T. Sato, Simulation study of a magnetohydrodynamic dynamo: convection in a rotating spherical shell, Phys. Fluids B 5 (8) (1993) 2793–2805.
[20] P.M. Gilman, J. Miller, Nonlinear convection of a compressible uid in a rotating spherical shell, Astrophys. J. Suppl. 61 (1986) 585–608.
[21] B. Fornberg, A pseudospectral approach for polar and spherical geometries, SIAM J. Sci. Comput. 16 (1995) 1071–1081.
[22] B. Fornberg, D. Merrill, Comparison of finite difierence- and pseudospectral methods for convective ow over a sphere, Geophys. Res. Lett. 24 (24) (1997) 3245–3248.
[23] J.P. Boyd, Chebyshev and Fourier Spectral Methods, second ed., Dover, New York, 2001.
[24] P. Merilees, The pseudospectral approximation applied to shallow water equations on a sphere, Atmosphere 11 (1973) 13–20.
[25] W.F. Spotz, M.A. Taylor, P.N. Swarztrauber, Fast shallow water equations solvers in latitude–longitude coordinates, J. Comput. Phys. 145 (1998) 432–444.
[26] R. Jakob-Chien, B.K. Alpert, A fast spherical filter with uniform resolution, J. Comput. Phys. 136 (1997) 580–584.
[27] N. Yarvin, V. Rokhlin, A generalized one-dimensional fast multipole method with application to filtering of spherical harmonics, J. Comput. Phys. 147 (1998) 594–609.
[28] R. Sadourny, A. Arakawa, Y. Mintz, Integration of the non-divergent barotropic vorticity equation with an icosahedral-hexagonal grid for the sphere, Mon. Weather Rev. 96 (1968) 351–356.
[29] J. Baumgardner, P. Frederikson, Icosahedral discretization of the two-sphere, SIAM J. Numer. Anal. 22 (1985) 1107–1115.
[30] F.X. Giraldo, A spectral element shallow water model on spherical geodesic grids, Int. J. Numer. Meth. Fluids 35 (2001) 869–901.
[31] H. Matsui, H. Okuda, Thermal convection analysis in a rotating shell by a parallel finite-element method – development of a thermal-hydraulic subsystem of GeoFEM, Concurrency Comput: Practice Exp 14 (2002) 465–481, doi:19.1002/cpe.625.
[32] R. Sadourny, Conservative finite-difierence approximations of the primitive equation on quasi-uniform spherical grids, Mon. Weather Rev. 100 (1972) 136–144.
[33] C. Ronchi, R. Iacono, P.S. Paolucci, The "cubed sphere": a new method for the solution of partial difierential equations in spherical geometry, J. Comput. Phys. 124 (1996) 93–114.
[34] M. Taylor, J. Tribbia, M. Iskandarani, The spectral element method for the shallow water equations on the sphere, J. Comput. Phys. 130 (1997) 92–108.
[35] F.X. Giraldo, J. Perot, P.F. Fischer, A spectral element semi-lagrangian (SESL) method for the spherical shallow water equations, J. Comput. Phys. 190 (2003) 623–650.
[36] E. Chaljub, Y. Capdeville, J.-P. Vilotte, Solving elastodynamics in a fluid–solid heterogeneous sphere: a parallel spectral element approximation on non-conforming grids, J. Comput. Phys. 152 (2003) 457–491.
[37] S.A. Orszag, Spectral methods for problems in complex geometries, J. Comput. Phys. 37 (1980) 70–92.
[38] M. Iskandarani, D. Haidvogel, J. Levin, A three-dimensional spectral element basin model for the solutions of the hydrostatic primitive equations, J. Comput. Phys. 186 (2003) 397–425.
[39] P.F. Fischer, N. Miller, H. Tufo, An overlapping Schwarz method for spectral element simulation of three-dimensional incompressible ows, in: P. Bjørstad, M. Luskin (Eds.), Parallel Solution of Partial Difierential Equations, Springer Verlag, Berlin, 2000, pp. 159–181.
[40] J. Blair Perot, An analysis of the fractional step method, J. Comput. Phys. 108 (1993) 51–58.
[41] S. Chandrasekhar, Hydrodynamic and Hydromagnetic Stability, Oxford University Press, Oxford, 1961.
[42] A.G. Tomboulides, Direct and large-eddy simulation of wake ows: flow past a sphere, Ph.D. thesis, Princeton University, 1993.
[43] J. Lopez, F. Marques, J. Shen, An eficient spectral-projection method for the Navier–Stokes equations in cylindrical geometries II. Three-dimensional cases, J. Comput. Phys. 176 (2002) 384–401.
[44] A. Fournier, H.-P. Bunge, R. Hollerbach, J.-P. Vilotte, Application of the spectral element method to the axisymmetric Navier–Stokes equation, Geophys. J. Int. 156 (2004) 682–700.
[45] G.E. Karniadakis, S.J. Sherwin, Spectral/hp Element Methods for CFD, Oxford University Press, Oxford, 1999.
[46] C. Bernardi, Y. Maday, A collocation method over staggered grids for the Stokes problem, Int. J. Numer. Meth. Fluids 8 (1988) 537–557.
[47] C. Bernardi, Y. Maday, Approximations spectrales de problfiemes aux limites elliptiquesMathfiematiques and Applications, vol. 10, Springer-Verlag, Paris, 1992.

[48] M.O. Deville, P.F. Fischer, E.H. Mund, High-order methods for incompressible fluid flowCambridge Monographs on Applied and Computational Mathematics, vol. 9, Cambridge University Press, Cambridge, 2002.

[49] E.M. Rnquist, Optimal spectral element methods for the unsteady three-dimensional incompressible Navier–Stokes equations, Ph.D. thesis, Massachusetts Institute of Technology, 1988.

[50] W. Gropp, E. Lusk, A. Skjellum, Using MPI: Portable Parallel Programming with the Message-Passing Interface, second ed., MIT Press, Cambridge, MA, 1999.

[51] P.F. Fischer, An overlapping Schwarz method for spectral element solution of the incompressible Navier–Stokes equations, J. Comput. Phys. 133 (1997) 84–101.

[52] H. Ma, A spectral element basin model for the shallow water equations, J. Comput. Phys. 109 (1993) 133–149.

[53] J.G. Levin, M. Iskandarani, D.B. Haidvogel, A nonconforming spectral element ocean model, Int. J. Num. Meth. Fluids 34 (2000) 495–525.

[54] M. Frigo, S.G. Johnson, The fastest fourier transform of the West, Tech. Rep. MIT-LCS-TR-728, Massachusetts Institute of Technology Laboratory for Computer Science, 1997.

[55] Y. Maday, D. Meiron, A.T. Patera, E.M. Rnquist, Analysis of iterative methods for the steady and unsteady Stokes problem: Application to spectral element discretizations, SIAM J. Sci. Comput. 14 (2) (1993) 310–337.

[56] W. Couzy, Spectral element discretization of the unsteady Navier–Stokes equations and its iterative solution on parallel computers, Ph.D. thesis, Ecole Polytechnique Fiedfierale de Lausanne, 1995.

[57] H. van der Vorst, BI-CGSTAB: A fast and smoothly converging variant of BI-CG for the solution of nonsymmetric linear systems, SIAM J. Sci. Statis. Comput. 13 (1992) 631–644.

[58] A.J. Chorin, Numerical solution of the Navier–Stokes equations, Math. Comput. 22 (1968) 745–762.

[59] G.E. Karniadakis, M. Israeli, S.A. Orszag, High-order splitting methods for the incompressible Navier–Stokes equations, J. Comput. Phys. 97 (2) (1991) 414–443.

[60] H. Blackburn, S. Sherwin, Formulation of a Galerkin spectral element – Fourier method for three-dimensional incompressible ows in cylindrical geometries, J. Comput. Phys. 197 (2004) 759–778.

[61] L.I.G. Kovasznay, Laminar ow behind a two-dimensional grid, Proc. Cambridge Phil. Soc. 44 (1948) 58–62.

[62] F.H. Busse, Homogeneous dynamos in planetary cores and in the laboratory, Annu. Rev. Fluid. Mech. 32 (2000) 383–408.

[63] E. Dormy, J.-P. Valet, V. Courtillot, Numerical models of the geodynamo and observational constraints, Geochemistry Geophysics Geosystems 1 (62).

[64] G.A. Glatzmaier, Geodynamo simulations – How realistic are they? Annu. Rev. Earth Planet. Sci. 30 (2002) 237–257.

[65] S.A. Orszag, On the elimination of aliasing in finite difference schemes by filtering high-wavenumber components, J. Atmos. Sci. 28 (1971) 1074.

[66] W. Malkus, Precession of the Earth as the cause of geomagnetism, Science 160 (1968) 259–264.

[67] J. Noir, D. Jault, P. Cardin, Numerical study of the motions within a slowly precessing sphere at low Ekman number, J. Fluid. Mech. 437 (2001) 283–299.

[68] P. Wessel, W. Smith, Free software helps map and display data, Trans. Am. Geophys. Union 72 (1991) 441–445.